Dissipative Locally Resonant Metasurfaces for Low-Frequency Rayleigh Wave Mitigation

Siqi Wang[a,b], Zhigang Cao[a,c,*], Qian Wu[b], Jiaji Chen[b], Yuanqiang Cai[a], Shaoyun Wang[b,*], Guoliang Huang[d,*]

[a]*Department of Civil Engineering and Architecture, Zhejiang University, Hangzhou 310058, China*
[b]*Department of Mechanical and Aerospace Engineering, University of Missouri, Columbia, MO 65211, USA*
[c]*Center for Balance Architecture, Zhejiang University, Hangzhou 310058, China*
[d]*Department of Mechanics and Engineering Science, Peking University, Beijing, 100871, China*

Abstract

Low-frequency Rayleigh waves from earthquakes, traffic, or heavy machinery pose significant risks to engineering structures, and how to mitigate subwavelength Rayleigh waves is a major challenge in the field. While attaching non-dissipative local resonators to the surface is a potential solution, its effectiveness is typically confined to narrow frequency ranges. This study proposes an elastic dissipative metasurface (EDM) for broadband mitigation and absorption, along with an energy analysis based on Poynting's theorem to quantify the wave scattering generated by EDMs. To realize broadband Rayleigh wave mitigation, we propose multi-resonant EDMs, where local resonators produce bandgaps at different frequencies, and damping bridges these gaps into a continuous broad bandgap. The working mechanism of the EMD to suppress broadband Rayleigh waves is revealed in a dissipative mass-in-mass lattice system through both negative effective mass density and effective metadamping coefficient. Furthermore, we design a graded EDM with slow modulation properties that eliminate scattered waves, achieving zero reflection, perfect rainbow absorption, and effective modulation of Rayleigh waves by leveraging the adiabatic theorem. The study can open new opportunities in the development of a new functional metasurface as an efficient wave mitigation material to suppress earthquake waves.

Keywords: Vibration mitigation, dissipative metasurfaces, Rayleigh wave ~~mitigation~~, energy absorption, ~~Elastic dissipative metasurfaces~~ local resonators, perfect rainbow absorption ~~micro-resonators design~~

1. Introduction

Mechanical metamaterials are engineered structural materials with mechanical properties rarely observed in natural materials. A hallmark of these materials is local resonance,

*Corresponding author

Email addresses: caozhigang2011@zju.edu.cn (Zhigang Cao), shaoyunwang@missouri.edu (Shaoyun Wang), guohuang@pku.edu.cn (Guoliang Huang)

characterized by subwavelength locally resonant inclusions or resonators [1, 2, 3, 4, 5, 6]. Typically, the degrees of freedom of these local resonators can be eliminated, allowing the background media to be modeled as an effective continuum with frequency-dependent mass densities and elastic moduli [7, 8, 9]. These effective properties can even be negative, leading to unconventional phenomena such as negative refraction [10, 11, 12], wave cloaking [13, 14, 15], and superlensing [16, 17]. The negative properties also create subwavelength bandgaps, providing a promising solution for low-frequency vibration and noise isolation, a challenge for traditional methods [18, 19, 20, 21].

The development of metamaterials has opened new possibilities for surface wave engineering, enabling control over Rayleigh waves generated by sources such as earthquakes, traffic, or heavy machinery. Traditionally, Rayleigh waves are mitigated using open and filled trenches [22, 23, 24, 25], wave barriers [26, 27, 28, 29, 30], piles [31, 32, 33, 34], and dampers [35, 36]. However, these conventional solutions are often bulky and ineffective for isolating low-frequency waves below 20 Hz. By installing resonators on the surface of a semi-infinite medium, it is possible to reduce Rayleigh wave transmission by creating a bandgap in the low-frequency range [37, 38, 39]. This approach has gained attention in various scenarios, including saturated soil substrates [40, 41], stratified substrates [42, 43], buried resonators [44, 45, 46], double resonators [47, 48], and nonlinear resonators [48, 49, 50, 51]. However, local resonance generates significant bulk waves and reflected Rayleigh waves, presenting unforeseen challenges. The impact of local resonance on Rayleigh wave scattering, as well as strategies to eliminate these unintended waves, remains unclear. Moreover, the development of an effective theory for multiple local resonances has not been reported, nor has the influence of negative effective mass function on surface wave decaying been thoroughly explored.

In addition to local resonances, damping significantly influences wave attenuation in materials, as it is still a challenge to study the reflection, dissipation and absorption of wave energy during the propagation of different types of waves ~~dissipates wave energy during propagation~~[52, 53, 54]. Local resonators with a small damping effect can reduce the amplitude of local resonance, decreasing reflection and enhancing wave transmission, while those with a large one can dissipate the wave energy, reducing transmission [48, 55, 56]. When Rayleigh waves pass through the semi-infinite medium with damped resonators, damping has a complex effect on wave scattering due to the existence of multiple wave types. This paper investigates the impact of damping in resonators on wave conversion and presents an energy analysis framework to reveal energy transformation patterns influenced by damping. Furthermore, multiple resonators can generate multiple subwavelength bandgaps [55], and significant damping can broaden the Rayleigh wave attenuation frequency range near these bandgaps [56]. The combination of multiple resonances and damping enables broad-frequency wave attenuation, a technique previously demonstrated for longitudinal waves [56, 57]. Here, we extend this approach to the Rayleigh wave system, achieving broad frequency attenuation with multiple damped resonators. Additionally, we introduce an effective metadamping coefficient to characterize the decay behavior using effective theory.

Uniform arrays of damped local resonators on the half space are unable to fully eliminate reflected surface and bulk waves. To address the issue, a spatially slow-varying structure is adopted. The field of space-varying or time-varying systems is emerging in science and engineering [58, 59, 60]. Novel phenomena in Rayleigh wave behavior have been observed using various spring-mass resonators and continuous resonant inclusions on substrate surfaces. For instance, non-reciprocal Rayleigh wave propagation has been achieved with space-time modulated springs, and the conversion of surface waves to shear waves and temporal rainbow trapping has been realized with time-varying springs [61, 62]. Additionally, topological edge modes and topological pumping of surface waves have been accomplished using space-varying springs [63, 64, 65, 66, 67, 68], and rainbow trapping for surface waves has been achieved using spatially varying resonators [69, 70, 71, 72]. In this study, we extend this concept to perfect rainbow absorption by employing spatially slow-varying damped resonators and further develop a rigorous theoretical framework for designing such resonators based on the adiabatic theorem [66]. Traditional unit cell analysis based on Bloch's theorem is commonly used to predict wave behavior in periodic systems. However, this approach is inadequate for space-varying systems [66, 73, 74]. Under adiabatic conditions, we leverage the adiabatic theorem and develop a local unit cell analysis method to predict wave behaviors in finite space-varying structures in both frequency and time domains.

~~In this paper, we focus on mitigating the impacts~~ This paper aims to mitigate the effects of low-frequency Rayleigh waves and scattered waves using elastic dissipative metasurfaces (EDMs) within a broadband frequency range. In Section 2, a semi-infinite elastic substrate with multiple attached resonators is simplified to a substrate with a single effective damped resonator using the effective theory. Subsequently, we develop a framework for calculating the dispersion relations of Rayleigh waves in this substrate incorporating the effective damped resonator. In Section 3, the results of the mitigation effect of EDMs with single resonance on Rayleigh waves are presented, exploring the impact of damping on complex bandgap structures, mode shapes, transmission spectra, conversion patterns, and wave field. Meanwhile, an energy analysis framework is established based on Poynting's theorem to quantify wave scattering from EDMs. In Section 4, we extend the analysis to EDMs featuring multiple resonators, achieving broad frequency range wave attenuation. Here, the effective mass and metadamping coefficients derived from the effective theory are used to efficiently characterize the decay behavior of Rayleigh waves, while the micro-resonators design is determined through inverse design. In Section 5, Rayleigh wave behaviors in spatially slow-varying EDMs are investigated to achieve the perfect rainbow absorption of all scattered waves. Additionally, a local unit cell analysis method based on the adiabatic theorem is developed to predict wave behavior in these structures. The paper concludes with final remarks and a summary of our findings in Section 6.

2. Models and Methods

To mitigate the propagation of Rayleigh waves on the ground, we employ novel EDMs composed of dissipative local resonators arranged on the soil surface, as illustrated in Fig. 1(a). The energy of the incident Rayleigh waves is distributed among four destinations: the energy of reflected Rayleigh waves, the energy of transmitted Rayleigh waves, the energy of bulk waves, and the energy absorbed by the EDMs. The objective of this study is to

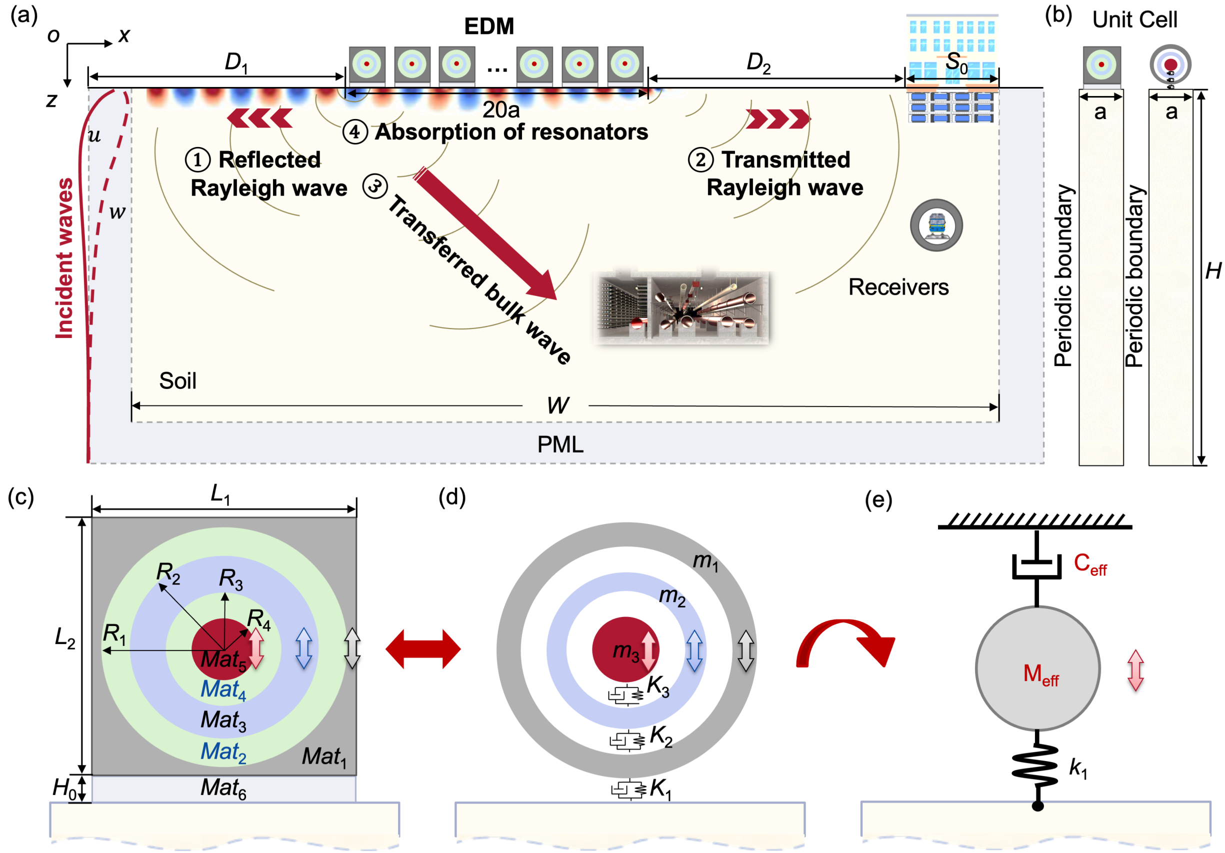

Figure 1: Schematic illustration of the EDMs for Rayleigh wave scattering mitigation. (a) Model depicting the four types of scattered energy from a 20-unit cell EDM, with the thickness of the PML being five times the wavelength, λ_R. (b) Unit cells of the EDM with physical resonators (left panel) and ideal resonators (right panel). (c) The geometry of physical resonators in the EDM. (d) The schematic diagram of ideal resonators. (e) The schematic diagram of the effective resonator model.

design EDMs that mitigate the influence of all scattered waves on infrastructures both on and below the surface, as depicted in Fig. 1(a).

2.1. Theory of Rayleigh waves in elastic dissipative metasurface

A schematic diagram illustrating the use of EDMs for mitigating scattered waves is shown in Fig. 1(a) and the unit cells of EDMs on the substrate are shown in Fig. 1(b). The elastic half-space has the following parameters: Young's modulus $E = 4.60 \times 10^7\,\mathrm{Pa}$, the Poisson's ratio $\mu = 0.25$, and the mass density $\rho = 1800\,\mathrm{kg/m^3}$. The width and height of the rectangular substrate are $W = 100a$ and $H = 20a$, respectively, where $a = 2.00$ m is the lattice constant representing the periodic spacing between adjacent resonators. Perfectly matched layers (PMLs) are applied to the bottom and side boundaries. An EDM consisting of 20 units is attached to the surface of the substrate, with distances D_1 and D_2 between the boundaries and the EDM both set to $40a$. The physical model of the local resonators, made of common engineering materials such as concrete (Mat_1), steel (Mat_3), lead (Mat_5), and rubber (Mat_2, Mat_4, and Mat_6), is depicted in Fig. 1(c). The material parameters for the model in Fig. 1(c) are specified as listed in Table 1.

Due to the substantially lower elastic constants of the connecting layers (springs) relative to the rigid bodies (masses), the physical system can be effectively approximated as an ideal hierarchical mass-spring-damper model, as depicted in Fig. 1(d). The governing equations for the three masses attached to the surface, expressed in the frequency domain, are formulated as follows:

$$m_1\omega^2 u_1(x) = K_1\left[u_1(x) - w(x,0)\right] + K_2\left(u_1(x) - u_2(x)\right), \tag{1a}$$

$$m_2\omega^2 u_2(x) = K_2\left[u_2(x) - u_1(x)\right] + K_3\left[u_2(x) - u_3(x)\right], \tag{1b}$$

$$m_3\omega^2 u_3(x) = K_3\left[u_3(x) - u_2(x)\right], \tag{1c}$$

where $u_1(x)$, $u_2(x)$ and $u_3(x)$ are the displacements of masses at position x, m_1, m_2 and m_3 are the masses of the resonators. The displacement of the substrate in the z-direction at position x when $z = 0$ is represented as $w(x, 0)$. The complex spring constants are defined as $K_j = k_j(1 + i\eta_j)$, $j = 1, 2, 3$, where k_1, k_2 and k_3 are springs stiffnesses, and η_1, η_2 and η_3 are the corresponding loss factors. The loss factor typically depends on the frequency and can be equivalently transformed into Rayleigh or viscous damping [75]. However, for simplicity, it is assumed to be a frequency-independent constant within the operating frequency range of 0 Hz to 26 Hz. This assumption is supported by experimental results for rubber [76], where the loss factor varies between 0 and 1.2.

The hierarchical mass-spring-damper model shown in Fig. 1(d) can be simplified to an effective mass-spring-damper model using effective theory, as illustrated in Fig. 1(e). The governing equation for the effective mass in Fig. 1(e) can be expressed as

$$m_{\text{eff}}\omega^2 u_1(x) = ic_{\text{eff}}\omega u_1(x) + K_1\left[u_1(x) - w(x,0)\right], \tag{2}$$

where m_{eff} is the effective mass and c_{eff} is the effective viscous coefficient, both of which are real numbers. To determine the effective mass and viscous coefficient, the variable vector $\mathbf{X} = [w(x,0), u_1(x), u_2(x), u_3(x)]^T$ is decomposed into two subspaces: $\mathbf{X} = [\mathbf{X}_1, \mathbf{X}_2]^T$, where $\mathbf{X}_1 = [w(x,0), u_1(x)]^T$ corresponds to the subspace of interest, and $\mathbf{X}_2 = [u_2(x), u_3(x)]^T$ comprises the variables to be eliminated. Using this separation, Eq. (1) can be reformulated as a set of matrix equations:

$$\begin{bmatrix}\mathbf{H}_{11} & \mathbf{H}_{12}\\ \mathbf{H}_{21} & \mathbf{H}_{22}\end{bmatrix}\begin{bmatrix}\mathbf{X}_1\\ \mathbf{X}_2\end{bmatrix} = \begin{bmatrix}0\\0\end{bmatrix}, \tag{3}$$

where

$$\begin{aligned}&\mathbf{H}_{11} = \begin{bmatrix}-K_1 & -m_1\omega^2 + K_1 + K_2\end{bmatrix}, \quad \mathbf{H}_{12} = \begin{bmatrix}-K_2 & 0\end{bmatrix},\\ &\mathbf{H}_{21} = \begin{bmatrix}0 & -K_2\\ 0 & 0\end{bmatrix}, \quad \mathbf{H}_{22} = \begin{bmatrix}-m_2\omega^2 + K_2 + K_3 & -K_3\\ -K_3 & -m_3\omega^2 + K_3\end{bmatrix}.\end{aligned} \tag{4}$$

Solving the second equation in Eq. (3), we obtain:

$$\mathbf{X}_2 = \mathbf{H}_{22}^{-1}\mathbf{H}_{21}\mathbf{X}_1. \tag{5}$$

Table 1: Material parameters of the local resonators [56]

Material number	Mat_1	Mat_2	Mat_3	Mat_4	Mat_5	Mat_6
Material	Concrete	Rubber1	Steel	Rubber2	Lead	Rubber3
Lamé constants, λ_s (Pa)	8.33×10^9	2.00×10^5	1.00×10^{11}	2.00×10^7	2.96×10^9	4.00×10^5
Lamé constants, μ_s (Pa)	1.25×10^{10}	1.00×10^5	8.20×10^{10}	1.00×10^5	5.60×10^8	2.00×10^5
Density, ρ_s (kg/m^3)	2.80×10^3	1.30×10^3	7.89×10^3	1.00×10^3	1.13×10^4	1.00×10^3

Substituting this expression into the first equation of Eq. (3) results in:

$$\mathbf{H}_{\text{eff}}\mathbf{X}_1 = 0, \tag{6}$$

where $\mathbf{H}_{\text{eff}} = \mathbf{H}_{11} - \mathbf{H}_{12}\mathbf{H}_{22}^{-1}\mathbf{H}_{21}$ is a 1 by 2 row vector, with its first element H_{eff}^1 equal to $-K_1$. Consequently, Eq. (6) can be rewritten as

$$K_1 \left[u_1(x) - w(x,0)\right] + \left(H_{\text{eff}}^2 - K_1\right) u_1(x) = 0, \tag{7}$$

where H_{eff}^2 is the second element of $\mathbf{H}_{\text{eff}}$. Since Eq. (7) is equivalent to Eq. (2), the effective mass m_{eff} and the effective viscous coefficient c_{eff} in Eq. (2) can be determined by comparing the coefficients of Eq. (2) and Eq. (7):

$$m_{\text{eff}} = -\frac{\text{Re}(H_{\text{eff}}^2 - K_1)}{\omega^2}, \tag{8a}$$

$$c_{\text{eff}} = \frac{\text{Im}(H_{\text{eff}}^2 - K_1)}{\omega}. \tag{8b}$$

Here, Re and Im represent the real and imaginary parts of a complex number, respectively. This concludes the construction of the effective mass-spring-damper model derived from the hierarchical mass-spring-damper system. Explicit expressions for calculating the effective parameters in Eq. (8) are provided based on the material parameters defined in Eq. (1). Although the derivation focuses on a hierarchical mass-spring-damper model with three resonators, the theoretical framework can be generalized to hierarchical systems with an arbitrary number of resonators.

On the surface of the substrate, the resonators apply point loads. Under the long-wavelength approximation, these point loads can be treated as uniformly distributed loads. As a result, the boundary conditions for normal stress σ_{zz} and shear stress σ_{xz} at the surface $z = 0$, where the resonators are attached, can be expressed as

$$\sigma_{zz}(x,0) = \frac{K_1}{a}\left[u_1(x) - w(x,0)\right], \tag{9a}$$

$$\sigma_{xz}(x,0) = 0. \tag{9b}$$

For the traveling wave, the wave solution of Rayleigh waves and resonators are expressed as [61, 77]

$$u_1(x) = U_1 e^{i(kx-\omega t)}, \tag{10a}$$

$$w(x,z) = k\left(-qAe^{-kqz} + iBe^{-ksz}\right)e^{i(kx-\omega t)}, \tag{10b}$$

$$\sigma_{zz}(x,z) = \mu k^2\left[2\left(rAe^{-kqz} - isBe^{-ksz}\right)\right]e^{i(kx-\omega t)}, \tag{10c}$$

$$\sigma_{xz}(x,z) = -\mu k^2\left[2iqAe^{-kqz} + rBe^{-ksz}\right]e^{i(kx-\omega t)}, \tag{10d}$$

where U_1, A, B are constants to be determined, ω is the angular frequency, k is the wavenumber, and the following relations hold:

$$q^2 - 1 + \left(\frac{c}{c_L}\right)^2 = 0, \quad s^2 - 1 + \left(\frac{c}{c_T}\right)^2 = 0, \quad r - 2 + \frac{c^2}{c_T^2} = 0, \tag{11}$$

where the wave speed $c = \omega/k$, the longitudinal wave speed is $c_L = \sqrt{\frac{\lambda+2\mu}{\rho}}$, and the shear wave speed is $c_T = \sqrt{\frac{\mu}{\rho}}$. Here, λ and μ are Lamé constants, and ρ is the density of the substrate. It is worth noting that the decay factors q and s must satisfy the following inequalities:

$$\mathrm{Re}(kq) > 0 \quad \text{and} \quad \mathrm{Re}(ks) > 0. \tag{12}$$

to ensure that the surface wave decays in the depth direction.

Substituting Eq. (10) and Eq. (11) into Eq. (9) yields the following system of linear homogeneous equations:

$$\begin{bmatrix} 2iq & r & 0 \\ \mu Lrk^2 + K_1kq & -2i\mu sLk^2 - iK_1k & K_1 \\ K_1kq & -iK_1k & -m_{\text{eff}}\omega^2 + ic_{\text{eff}}\omega + K_1 \end{bmatrix} \begin{bmatrix} A \\ B \\ U_1 \end{bmatrix} = \begin{bmatrix} 0 \\ 0 \\ 0 \end{bmatrix}. \tag{13}$$

Eq. (13) can be compactly expressed in matrix form as $\mathcal{H}(\omega, r, q, s, k)\mathbf{U} = 0$. The dispersion relation $k(\omega)$ is determined by vanishing the determinant of the coefficient matrix:

$$\det(\mathcal{H}) = 0. \tag{14}$$

To derive the dispersion relation, the angular frequency ω is specified in advance, while other variables remain unknown. In a non-dissipative system, where all variables and polynomial equations are real, the system can be solved easily by eliminating variables. In this case, the wavenumber k is real, corresponding to propagating Rayleigh waves. Nevertheless, in our dissipative system composed of masses and damped springs, all variables and polynomial equations are complex, complicating the process of solving these equations.

To address the complexity of solving Eqs. (11) and (14), a resultant-based elimination theory from computational algebraic geometry is introduced to ensure precise and efficient solutions [78]. The left-hand sides of Eqs. (14) and (11) are defined as polynomials $p_1(r,q,s,k)$, $p_2(q,k)$, $p_3(s,k)$, and $p_4(r,k)$, respectively. For a given ω, the resultant of p_1 and p_2 with respect to q eliminates the variable q, yielding a new polynomial:

$$p_5(r,s,k) = \mathrm{Res}(p_1, p_2, q), \tag{15}$$

where Res is the resultant function, as defined in Appendix A. Similarly, taking the resultant of p_5 and p_3 with respect to s eliminates the variable s and gives a new polynomial:

$$p_6(r,k) = \mathrm{Res}(p_5, p_3, s). \tag{16}$$

Finally, taking the resultant of p_6 and p_4 with respect to r eliminates variable r and gives a new polynomial:

$$p_7(k) = \mathrm{Res}(p_6, p_4, r). \tag{17}$$

The polynomial $p_7(k)$ is related solely to the wavenumber, enabling its roots to be determined accurately using the "roots" function in MATLAB. To ensure physically meaningful results, redundant roots are discarded based on the inequalities in Eq. (12). For each valid root k, the corresponding q and s are determined using the resultant method similarly. Roots are retained only if the real parts of both q and s are positive; otherwise, they are discarded. By sweeping the frequency within a specified range and calculating the root k using the resultant method, the dispersion curves can be obtained completely and precisely.

2.2. Finite element method analysis

All simulations are performed by using the finite element method (FEM) in COMSOL Multiphysics. For the calculation of k-ω dispersion curves of the continuous model shown in the left panel of Fig. 1(b), we use the partial differential equations (PDEs) of elasticity based on Bloch's theorem to capture the real and imaginary components of the wavenumber. These PDEs are solved using the "Coefficient Form PDE Interfaces." Specifically, Bloch periodic boundary conditions are applied to the left and right boundaries of the unit cell to ensure infinite periodicity, and an eigenfrequency analysis is conducted to extract the complex wavenumbers for a given angular frequency ω. The real part of the wavenumber represents the propagating wave's spatial oscillation, while the imaginary part corresponds to the attenuation along the propagation direction. This approach enables accurate characterization of both propagating and evanescent wave modes in the metasurface. For the calculation of k-ω dispersion curves of the discrete unit cell shown in the right panel of Fig. 1(b), ~~the "Global ODEs and DAEs Interface" is also utilized to describe~~ we utilized both the "Global ODEs and DAEs Interface" in COMSOL and the effective mass-spring-damper system described in Eq. (2) for rapid bandgap predictions. For analyzing Rayleigh wave scattering depicted in Fig. 1(a), "Structural Mechanics Module" and "Global ODEs and DAEs Interface" in the frequency domain are used. The FEM simulations in these cases account for the coupling between the substrate and the resonators to evaluate the wave propagation and attenuation characteristics.

For a given frequency (swept from 0 Hz to 26 Hz), the displacement distribution at the left boundary of PML is prescribed as

$$u = re^{-kqz} + 2sqe^{-ksz}, \tag{18a}$$

$$w = iq\left(re^{-kqz} - 2e^{-ksz}\right), \tag{18b}$$

in the frequency domain to selectively excite a Rayleigh wave without generating any bulk waves, as shown in Fig. 1(a). Here, q, s, and k are determined by solving Eq. (14) and

Eq. (11) for the given frequency in the absence of attached resonators. The complex form of $w(z)$ captures the amplitude and phase of Rayleigh waves. The exponential decay terms e^{-kqz} and e^{-ksz} ensure surface energy confinement, waves, distinguishing them from the deep propagation behavior of bulk waves. This complex representation ensures that pure Rayleigh waves are excited while effectively avoiding interference from bulk waves.

To analyze the transmitted Rayleigh wave, the frequency response function (FRF) is defined as

$$\mathrm{FRF} = \frac{20}{S_0} \log_{10} \left(\int_{S_0} \frac{|w|}{|w_0|} \, dx \right), \tag{19}$$

where S_0 is the length of the surface receiver in Fig. 1(a), w (w_0) is the displacement component along the z-direction calculated from the model with (without) the EDM.

3. Mitigation of Rayleigh wave scatterings by EDMs with single local resonance

In this section, we start with the simplest model, employing an EDM with single local resonators to attenuate transmitted Rayleigh waves. The resonators have a stiffness of $k_1 = 1.9 \times 10^7$ N/m and a mass of $m_1 = 2000$ kg. We use both dispersion relations and FRF to characterize wave transmission. Additionally, an energy analysis provides deeper insights into the complex interactions between Rayleigh waves and the EDM. In this analysis, we decompose the bulk waves into P and SV waves and examine wave mode conversion in the bulk using a 2D Fourier transform (FT). The damping effect on Rayleigh wave scattering is considered throughout this section.

3.1. Dispersion analysis and transmitted Rayleigh waves mitigation

First, we calculate the dispersion curves presented in the left panels of Figs. 2(a-d). The dispersion curves of the Rayleigh wave, obtained from finite element method (FEM) analysis (purple) and analytical approach from Eq. (14) (orange), are in excellent agreement, confirming the accuracy of the analytical model. In this case, we have $k_2 = k_3 = m_2 = m_3 = \eta_2 = \eta_3 = 0$ and define η_1 as η.

In the absence of damping ($\eta = 0$), the dispersion bands of Rayleigh waves are all real, and a bandgap emerges due to the local resonance. The mode shapes of the highlighted modes A, B, and C are shown in Fig. 2(e), which demonstrate an exponentially decaying field intensity in the depth direction. When damping is presented ($\eta \neq 0$), the imaginary parts of dispersion curves are non-zero, while the real parts of dispersion curves bend for small damping or connect to higher frequency bands for larger ones. The imaginary dispersion indicates a decaying Rayleigh wave, where the decay factor is proportional to the imaginary wavenumber. It is noteworthy that even though the Rayleigh band warps into the sound cone, it still belongs to a Rayleigh wave mode rather than a bulk mode, as illustrated in Fig. 2(e) mode D. The mode shapes at point D exhibit characteristic vertical and horizontal displacement components of Rayleigh waves, which are distinct from bulk wave modes that lack such coupled surface behavior. Moreover, the energy associated with these modes remains predominantly confined to the surface, further supporting their classification as Rayleigh wave modes. The warping into the sound cone is primarily caused by the coupling

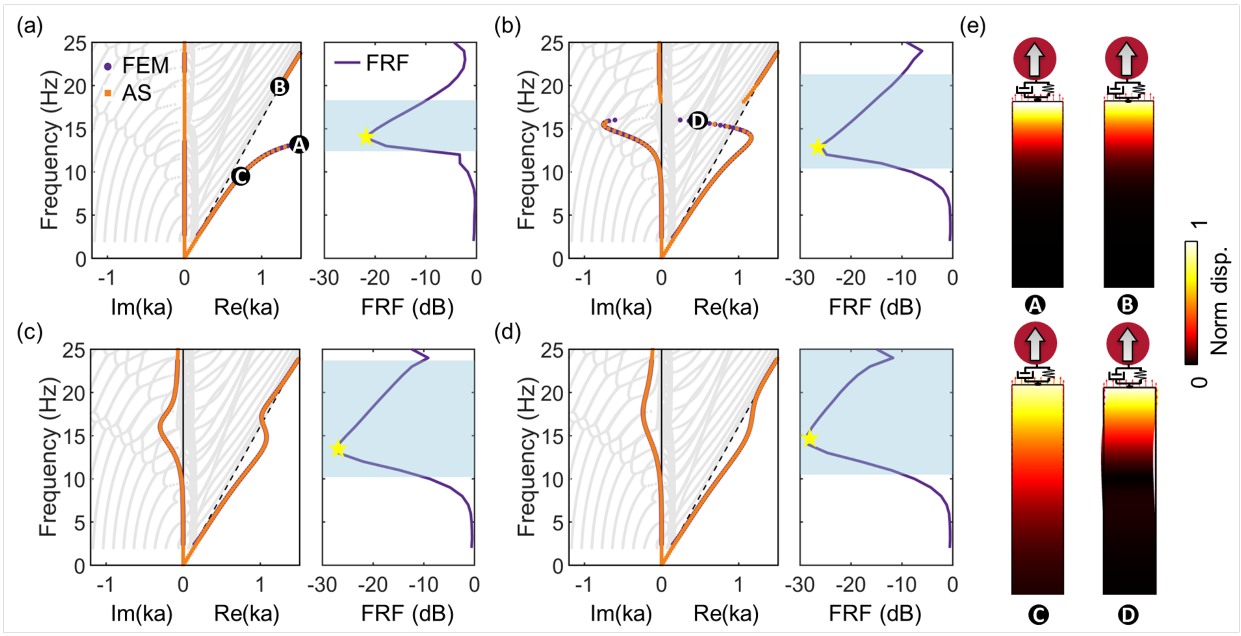

Figure 2: Complex dispersion curve diagrams, transmission FRF, and mode. (a)-(d) Dispersion diagrams and FRF for the loss factor $\eta = 0, 0.3, 0.6,$ and 0.9, respectively. In the left panels of (a)-(d), the gray curves correspond to bulk waves from FEM unit cell analysis, whereas the purple (FEM analysis) and orange curves (analytical solution (AS) described in Section 2) represent the complex dispersion curves of Rayleigh waves. In the right panels of (a)-(d), the light blue region represents the stopband with < -10 dB transmission. (e) Corresponding mode shapes of the four eigenmodes A, B, C, and D highlighted in panels (a) and (b).

between the Rayleigh wave and the dissipative effects introduced by the metasurface. This interaction modifies the dispersion curve without altering the fundamental nature of the mode, highlighting the unique dynamics of the metasurface system.

To fully capture the transmission property of the EDM, we show the FRF results in the right panels of Figs. 2(a-d). Here, we define the effective stopband as the light blue region where the FRF is less than -10 dB. The effect of damping on the stopband range and the minimum FRF is shown in Fig. 3. We can observe that a higher loss factor simultaneously enhances the bandwidth of the stopband and decreases the minimum transmission, leading to significantly suppressed transmission.

3.2. Energy analysis of Rayleigh wave scatterings by EDMs

The energy of the incident Rayleigh wave is transformed into four distinct parts by EDMs. To quantitatively characterize the energy transformation, we employ an energy analysis method based on the concept of frequency-dependent elastic energy flux $\mathbf{I}$, or elastic Poynting's vector, defined as [78, 79]

$$\mathbf{I} = -\frac{1}{2}\mathrm{Re}(\boldsymbol{\sigma}^* \cdot \mathbf{v}), \tag{20}$$

where $\boldsymbol{\sigma}$ is the stress tensor, $(\cdot)^*$ is the complex conjugate operator, $\mathbf{v}$ is the velocity vector. The energy of reflected Rayleigh wave E_r, transmitted Rayleigh wave E_t, scattered bulk

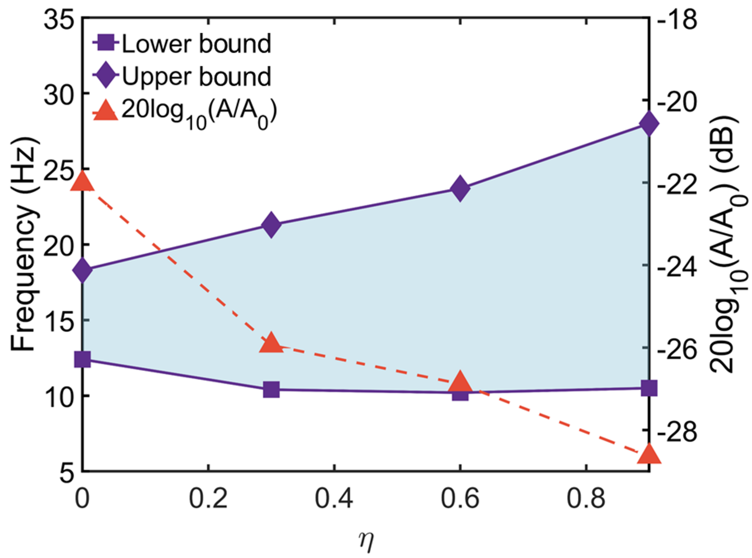

Figure 3: The bandwidth at -10 dB (purple region) and minimum FRF (orange dashed line) in the function of loss factor η. The data are obtained from the right panels of Figs. 2(a-d).

wave E_b, and dissipation from resonators E_l are defined as the following:

$$E_r = E_i + \int_{S_1} \mathbf{I} \cdot \mathbf{n} dS, \tag{21a}$$

$$E_t = \int_{S_2} \mathbf{I} \cdot \mathbf{n} dS, \tag{21b}$$

$$E_b = \int_{S_3} \mathbf{I} \cdot \mathbf{n} dS, \tag{21c}$$

$$E_l = \frac{1}{2} \int_{S_4} \mathrm{Re}(\boldsymbol{\sigma}^* : i\omega\boldsymbol{\epsilon}) dS, \tag{21d}$$

where $\mathbf{n}$ is the unit vector pointing in the direction of the outward normal, $\boldsymbol{\epsilon}$ is the strain tensor, and the energy of incident Rayleigh wave is $E_i = |\int_{S_1} \mathbf{I}_i \cdot \mathbf{n} dS|$. Here, $\mathbf{I}_i$ is the energy flux of the incident Rayleigh wave which can be calculated from the homogeneous elastic medium in the absence of EDMs. The integral $\int_{S_1} \mathbf{I} \cdot \mathbf{n}\, dS$ represents the total energy flux (incident and reflected waves) on S_1. This equation is derived from the conservation principle, ensuring that all energy entering or leaving the boundary S_1 is accounted for. Additionally, the definition of surfaces S_1, S_2, S_3, and S_4 can be found in the inset of Fig. 4(a).

According to Poynting's theorem, the energy of an incident Rayleigh wave E_i is equal to the summation of the energy of the transmitted Rayleigh wave E_t, reflected Rayleigh wave E_r, scattered bulk wave E_b, and absorption by resonators E_l. This can be expressed as:

$$E_i = E_r + E_t + E_b + E_l. \tag{22}$$

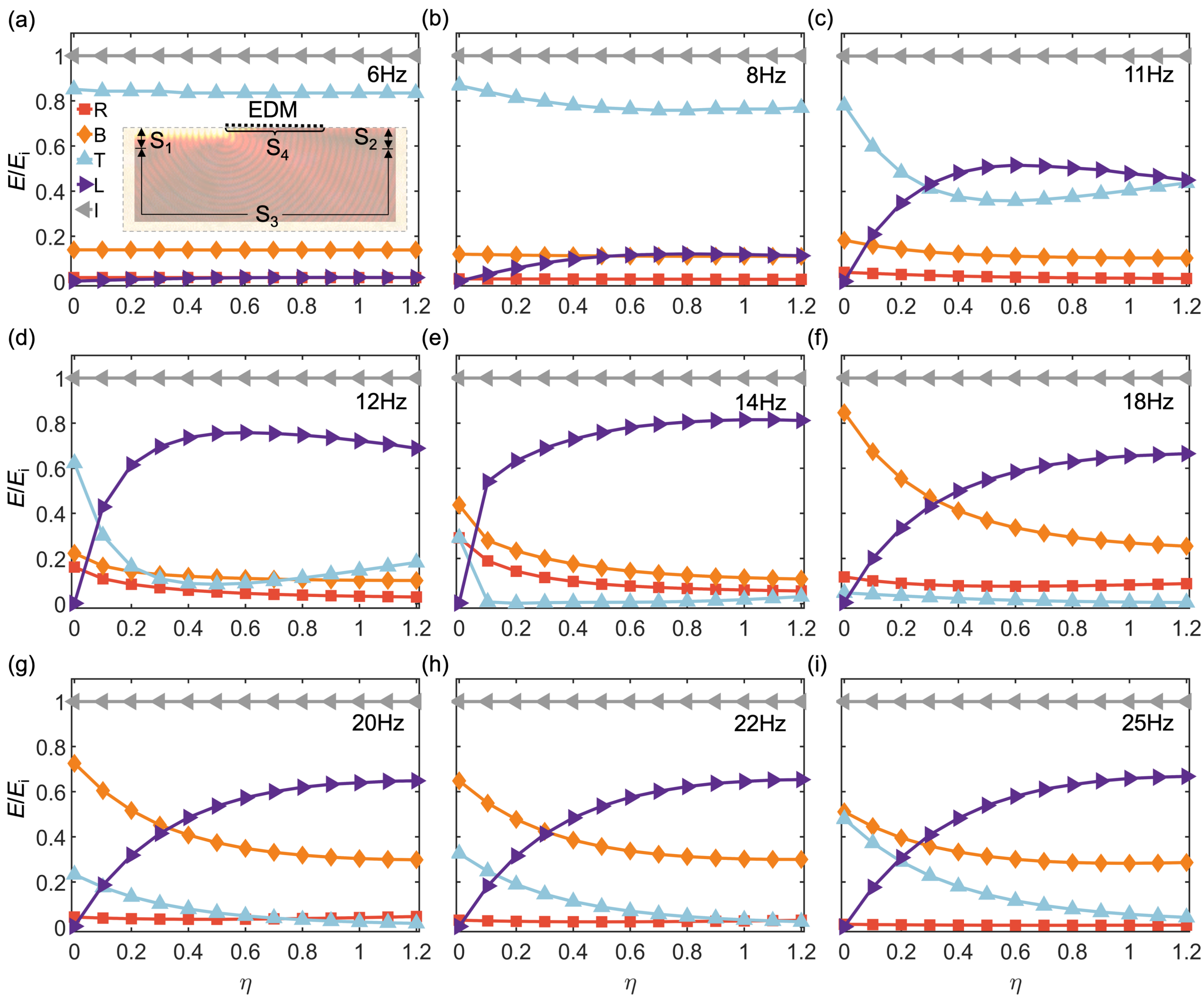

Figure 4: The energy (E) normalized by the incident energy is categorized as reflected Rayleigh wave (R), transferred bulk wave (B), transmitted Rayleigh wave (T), resonator absorption (L), and incident wave (I) with respect to different loss factors and different frequencies. S_1, S_2, S_3, and S_4 are the regions for calculating the energy of reflected Rayleigh wave, transmitted Rayleigh wave, bulk waves, and absorption by the EDM.

In Fig. 4, we illustrate how each energy component is influenced by the loss factor and the frequency near the stopband (6 Hz to 25 Hz). Incident energy is normalized for convenience. At frequencies below 8 Hz, Rayleigh waves exhibit a long penetration depth, leading to minimal energy confinement at the surface and limited interaction with the resonators. Consequently, the majority of energy (85%) is transmitted, while the remaining energy (15%) is scattered into bulk waves at the left interface of the EDM. These energy ratios are largely independent of the loss factor, as demonstrated in Fig. 4(b). As the frequency reaches 8 Hz, the penetration depth of Rayleigh waves decreases, increasing interaction with the resonators. The incident wave energy begins to dissipate through the resonators. As the frequency approaches the resonant frequency (13.5 Hz), the coupling between Rayleigh

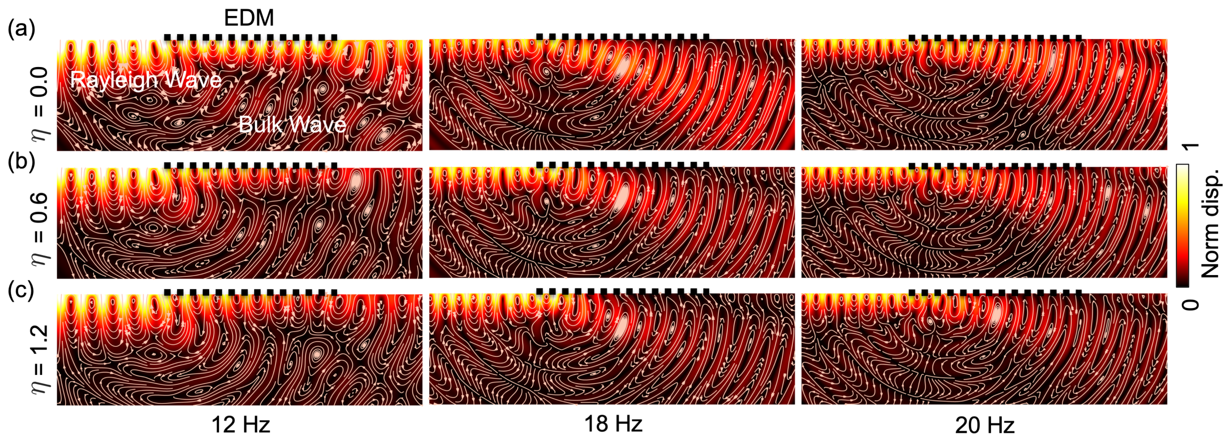

Figure 5: The wave scattering field of an incident Rayleigh wave at frequencies 12 Hz, 18 Hz, and 20 Hz, and loss factors (a) $\eta = 0.0$, (b) $\eta = 0.6$, and (c) $\eta = 1.2$.

waves and local resonance becomes more pronounced, and energy flows in all four directions, as shown in Figs. 4(c-d). At 12 Hz, the energy of the Rayleigh wave dissipates significantly as η increases, as shown in the left panels in Fig. 5. It is noteworthy that the decay factor of the Rayleigh wave does not vary monotonically with the loss factor, as demonstrated in Fig. 2. As a result, we can observe a decrease in transmitted wave energy followed by an increase in Fig. 4(d).

For EDM operating within the bandgap (13.5 to 19 Hz) with $\eta = 0$, the energy of the reflected wave and bulk waves dominates, with minimal transmitted wave energy, as the Rayleigh wave cannot propagate within the bandgap, as shown in Figs. 4(e-f). As η increases, the loss factor reduces resonance and introduces the horizontally decaying Rayleigh waves, causing an increase in dissipated energy while other energies decrease, as observed in the middle panels of Figs. 5(a-c). When the frequency exceeds the upper bound of the bandgap, the impact of local resonance diminishes, leading to a decrease in bulk wave energy and an increase in transmitted wave energy. In this region, the loss factor further diminishes bulk waves and Rayleigh wave energies in the EDM, resulting in decreased energies of both bulk waves and transmitted waves as η increases, as depicted in the right panels of Figs. 5(a-c). Figure 4 illustrates that without damping, local resonance significantly reduces transmitted wave energy but introduces other scattered waves in the bandgap region (13.5 to 19 Hz). The damping in the local resonators greatly reduces these scattered waves near the bandgap region (12 to 19 Hz). If the damping is substantial, the transmitted wave can also be eliminated above the bandgap, though bulk waves cannot be entirely mitigated.

We can conclude that EDM with single local resonances effectively attenuates Rayleigh waves with the correct combination of frequency, loss factor, and energy distribution. While the effect is weak at extremely low frequencies, a slight increase in the loss factor at mid-frequencies significantly enhances energy dissipation through resonator absorption. At high frequencies, the effect stabilizes, but excessive damping can reduce energy conversion efficiency. The EDM effectively converts Rayleigh wave energy into other forms, primarily via

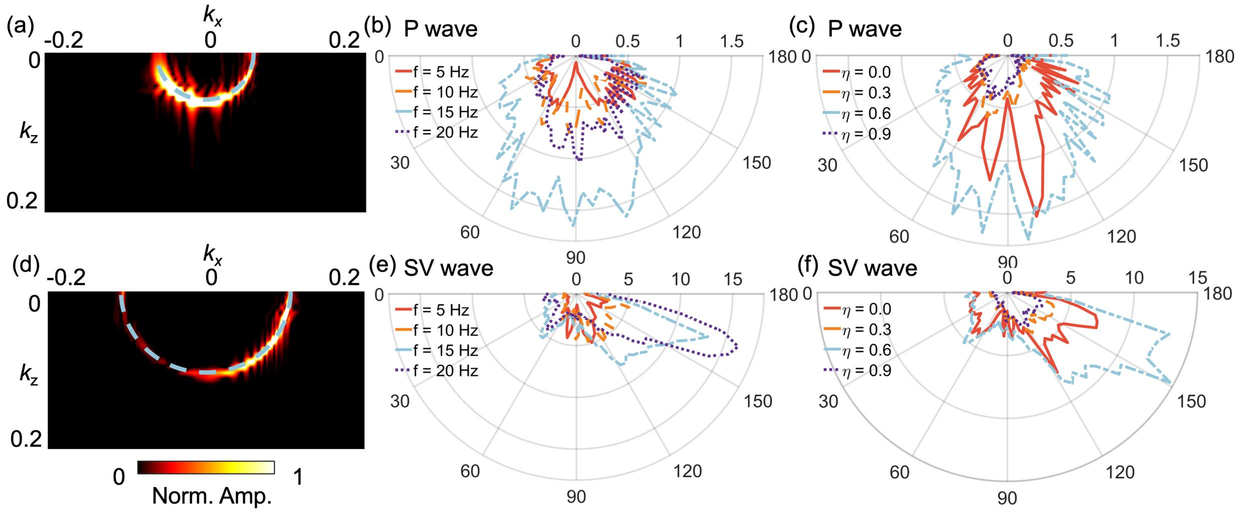

Figure 6: Angle analysis of transferred P and SV waves. (a) The 2D FT of the divergence of the displacement field (P wave) at a frequency of 12 Hz and a loss factor of 0.3. (b) The polar diagram of the transferred P wave with a loss factor of 0 across different frequencies. (c) The polar diagram of the transferred P wave at 12 Hz for varying loss factors. (d) The 2D FT of the curl of the displacement field (SV wave) at a frequency of 12 Hz and a loss factor of 0.3. (e) The polar diagram of the transferred SV wave with a loss factor of 0 across different frequencies. (f) The polar diagram of the transferred SV wave at 12 Hz for varying loss factors.

bulk wave conversion and resonator absorption. This conversion mechanism is influenced by both the frequency of the incident waves and the damping properties of the EDM.

3.3. Bulk waves decomposition

In the current system, bulk waves consist of both P and SV waves. We decompose bulk waves into P and SV waves and discuss each of their propagation. P and SV waves are separated by taking the divergence and curl of the displacement field, respectively. The primary propagation direction is determined by performing a 2D FT on the divergence and curl, as illustrated in Figs. 6(a,d) for a frequency of 12 Hz and $\eta = 0.3$. By integrating the amplitude in the 2D reciprocal space along the radial direction, we obtain polar diagrams for different frequencies and loss factors, depicted in Figs. 6(b,c,e,f). In these figures, the magnitude of P waves is significantly smaller than that of SV waves, indicating that SV waves dominate the bulk waves scattered by the EDM (Figs. 6(a,d)). In Figs. 6(b-c) and 6(e-f), P waves are primarily propagating along z direction, while SV waves have a larger component in x direction. The magnitude of P and SV waves decreases with increasing damping near the resonance frequency, indicating that damping effectively reduces these waves. These analyses reveal that Rayleigh-to-bulk wave conversion primarily results in z-propagating P waves and predominantly x-propagating SV waves. The result can be helpful in determining underground wave types, providing insights into the design of underground devices. Furthermore, the loss factor significantly reduces bulk waves near the resonance frequency, underscoring its importance in wave mitigation strategies.

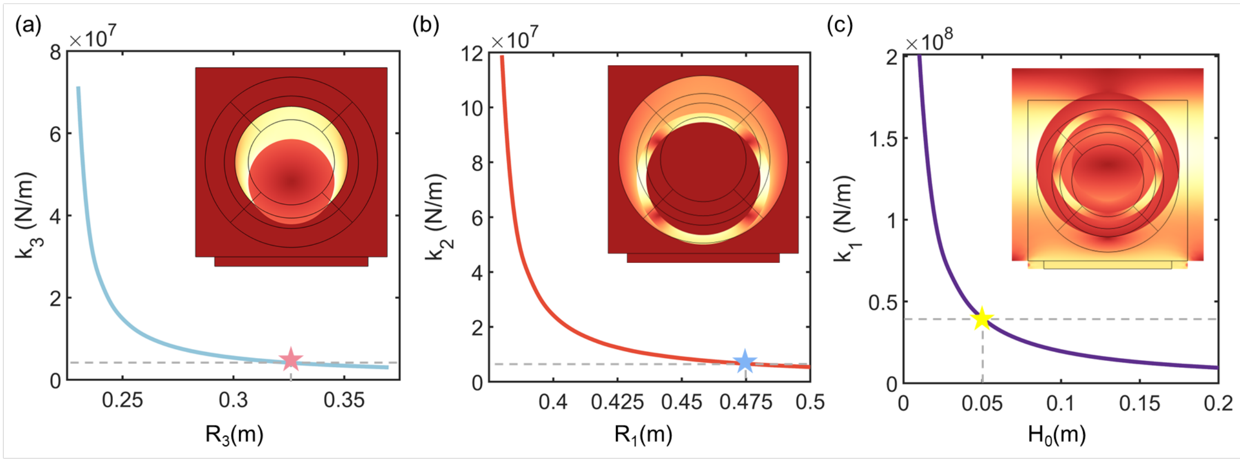

Figure 7: Stiffness of EDMs with three resonators (k_1, k_2, and k_3) under numerical tests and the optimal design corresponding to the actual structural geometry: (a) the intermediate resonator radius R_3, (b) the outermost resonator radius R_1, and (c) the element side length H_0.

4. Rayleigh wave mitigation by multi-resonant EDMs

4.1. Resonators design and dispersion analysis

As previously discussed, EDMs are highly effective in attenuating transmitted Rayleigh waves near their resonance frequencies. When equipped with multiple resonators, EDMs can mitigate Rayleigh waves near these specific resonance frequencies but cannot effectively block the Rayleigh waves far from these frequencies. However, damping can broaden the resonance peaks, resulting in broadband attenuation of transmitted Rayleigh waves. In this section, we examine EDMs with three dissipative resonators. The mass-spring parameters listed in Table 2 and the geometric parameters of the physical model shown in Fig. 1(c) listed in Table 3 are determined inversely by numerical tests in Fig. 7.

The mass m_3 and its density are known, allowing the radius R_4 to be determined from its volume. Subsequently, for a given R_3, a displacement is applied to the mass m_3 while the mass m_2 remains fixed, and the resulting reaction force is extracted in COMSOL. The stiffness k_3 is then calculated as the ratio of the reaction force to the prescribed displacement. By varying the radius R_3, the relationship between k_3 and R_3 is established and plotted in Fig. 7(a). For a specific k_3, the corresponding geometric parameter R_3 is determined using a graphical method. Next, R_2 is determined from its volume, and the geometric parameter R_1 is identified using the graphical method shown in Fig. 7(b). Here, the stiffness k_2 is calculated by fixing the mass m_1 and applying a prescribed displacement to m_2 for a given R_1. Finally, R_1 is determined from its volume, and the geometric parameter H_0 is identified using the graphical method shown in Fig. 7(c). In this case, the stiffness k_1 is calculated by fixing the substrate and applying a prescribed displacement to m_1 for a given H_0.

We then discuss the dispersion curves, mode shapes, and the effect of damping on the discrete and continuous models. The dispersion curves of the analytical model (orange) and the continuous model (purple) are illustrated in Fig. 8(a), with corresponding mode shapes shown in Figs. 8(b) and 8(c), respectively. As shown in Fig. 8(a), within the frequency range

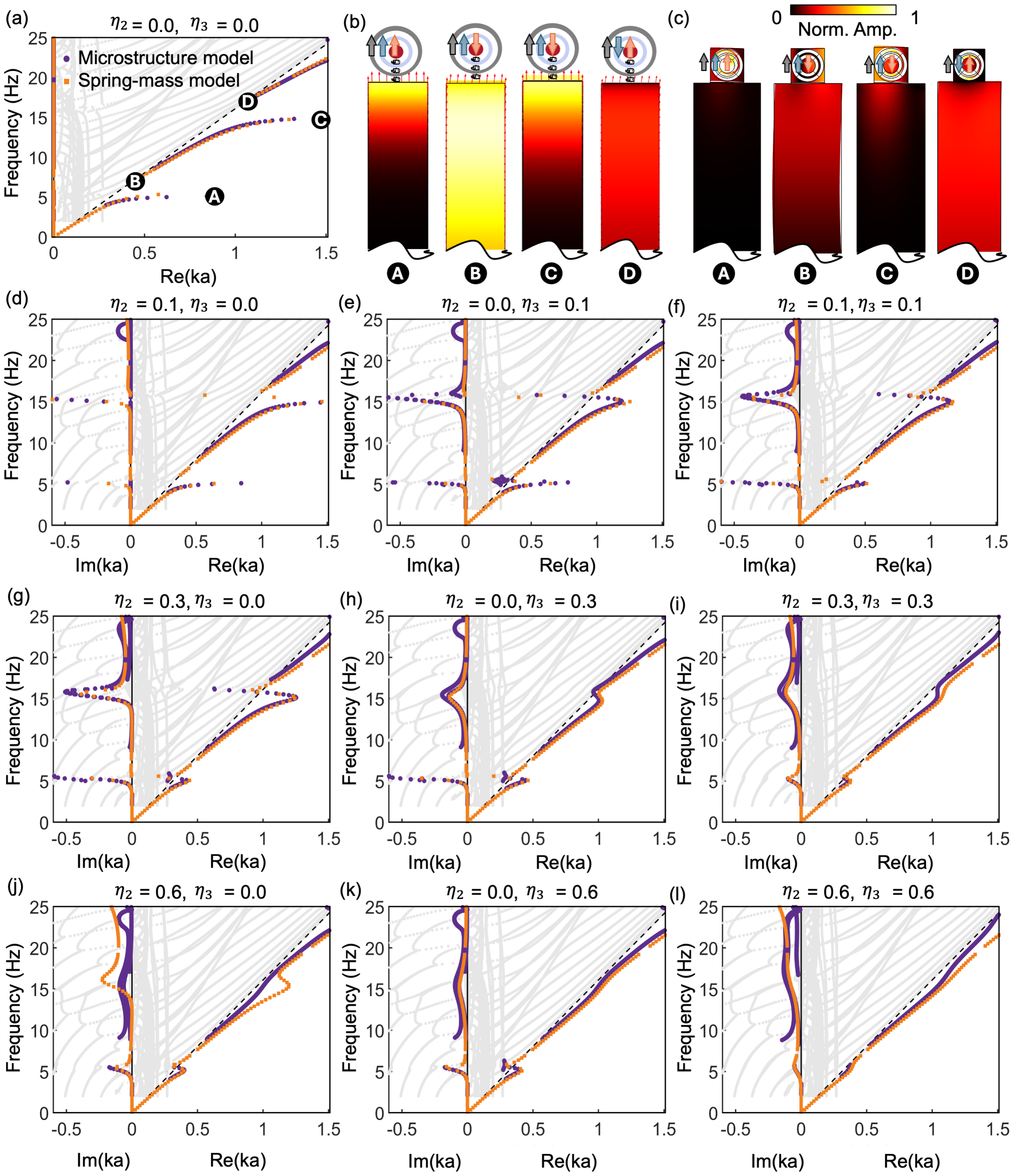

Figure 8: (a) Dispersion curves of the EDM with an array of triple damped resonators for $\eta_2 = \eta_3 = 0$. The gray curves are dispersion curves of bulk waves from unit cell analysis, whereas purple curves (continuous model analysis) and orange curves (analytical method described in section 2) represent dispersion curves of Rayleigh waves. (b-c) The mode shapes. (d-l) Dispersion curves of EDMs with an array of triple-damped resonators for different combinations of η_2 and η_3.

Table 2: Parameters of local resonators.

Mass of resonator	**Value (kg)**	**Stiffness of resonator**	**Value (N/m)**
m_1	989	k_1	3.98×10^7
m_2	1128	k_2	6.58×10^6
m_3	1890	k_3	4.17×10^6

Table 3: Geometrical parameters of the local resonators.

Parameters	a	L_1	L_2	H_0	R_1	R_2	R_3	R_4
Length (m)	2.00	1.00	1.00	0.05	0.475	0.375	0.325	0.225

of interest, two bandgaps are generated by the local resonators m_2 and m_3. In contrast, the resonance frequency of m_1 is well above 25 Hz, placing the bandgap associated with this resonator significantly outside the frequency range of interest.

For different combinations of loss factors η_2 and η_3 (0.3, 0.6, and 0.9, respectively), Figs. 8(d-f) show that loss factor η_2 affects the resonance at higher frequencies, whereas loss factor η_3 affects the resonance at lower frequencies. Increasing the loss factors η_2 or η_3 significantly broadens the peaks in imaginary parts, and simultaneously increasing both factors links those two imaginary peaks, enabling broadband attenuation of Rayleigh waves in EDMs.

4.2. Effective model

Now, we turn to describe the behavior of the effective mass m_{eff} and effective damping c_{eff}, which can be utilized to quickly predict the dispersion curves and the decaying behavior of Rayleigh waves in EDMs. In Fig. 9, the resonance of two inner resonators induces two sharp peaks and two sharp valleys in the effective mass when damping is small. At these valleys, the effective mass becomes negative. Negative mass regions are not perfectly aligned with the bandgap regions in the dispersion curves but are very close due to the influence of bulk waves. Consequently, the bandgaps in the dispersion curves can be approximately predicted by identifying the negative mass region under low damping conditions. As damping increases, it broadens the width and reduces the height of c_{eff} peaks, as shown in Fig. 9. The width of both peaks increases with an increment in either η_2 or η_3, as depicted in Figs. 9(a-b). Notably, η_2 significantly broadens the higher frequency peak while only slightly affecting the lower frequency one. On the other hand, η_3 predominantly contributes to the broadening of the lower frequency peak. When both η_2 and η_3 are large, the c_{eff} peaks merge, forming a continuous response over a broad frequency range (5 to 25 Hz). When compared with Fig. 8, the influence of c_{eff} mirrors its effect on the imaginary component of the dispersion curves, particularly when damping is significant. Therefore, effective damping c_{eff} can quickly predict the imaginary part of the dispersion curves and the decaying behavior of Rayleigh waves in EDMs.

4.3. Transmission analysis in the frequency domain

The imaginary component of the dispersion curves governs the decaying factor of Rayleigh waves within the EDMs. If the Rayleigh waves decay rapidly, the transmitted wave is min-

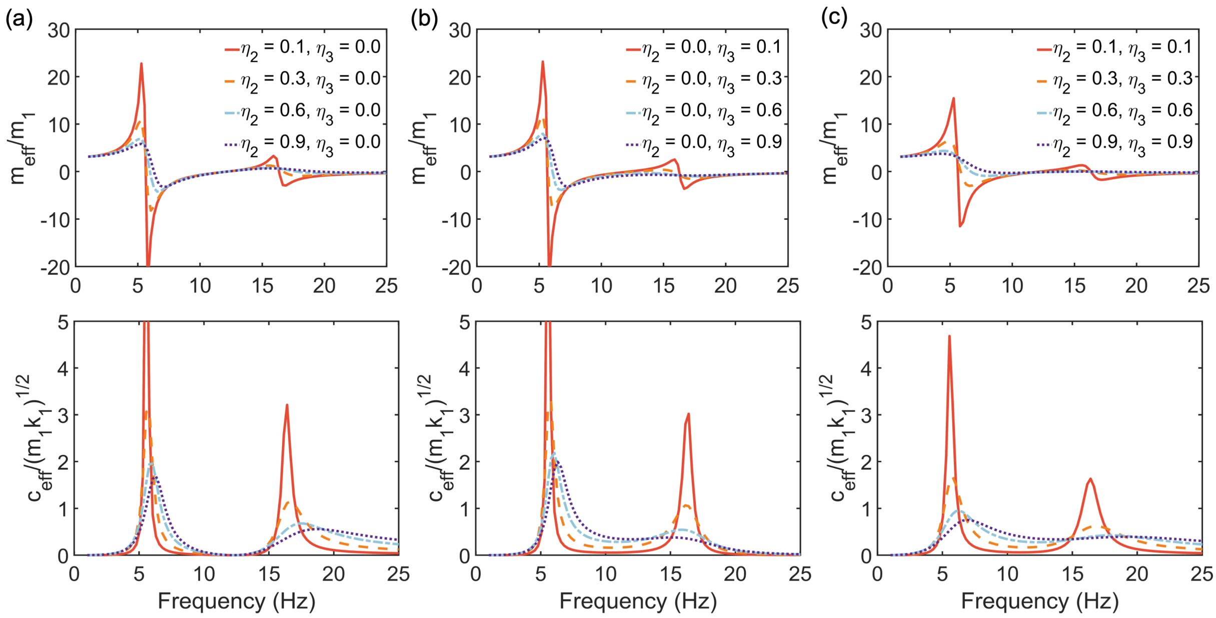

Figure 9: Effective mass and effective metadamping coefficient of EDM lattice system with three resonators with different loss factors: (a) $\eta_2 = 0.1, 0.3, 0.6, 0.9$; $\eta_3 = 0.0$, (b) $\eta_3 = 0.1, 0.3, 0.6, 0.9$; $\eta_2 = 0.0$, and (c) $\eta_2 = \eta_3 = 0.1, 0.3, 0.6, 0.9$.

imal. However, this factor alone is insufficient to quantitatively predict the transmitted wave, as it does not account for the presence of scattered waves. Therefore, we analyze the FRF in the frequency domain to obtain the effect of damping on transmitted waves. In Fig. 10(a), the first stopband widens as loss factor η_2 increases, but the attenuation amplitude initially increases before subsequently decreasing. In Fig. 10(b), a high-frequency stopband rapidly forms, significantly enhancing wave attenuation, though low-frequency attenuation diminishes with increasing η_3. When η_2 and η_3 increase simultaneously, all bands merge to form a complete stopband (see Fig. 10(c)).

Figure 10(d-g) depicts the scattering fields of an incident Rayleigh wave at various frequencies (6 Hz, 15 Hz, and 23 Hz) for different EDM loss factors. It can be observed that after passing through the non-dissipative metasurface ($\eta_2 = \eta_3 = 0$), the Rayleigh wave shows a significant reduction in transmission at 6 Hz and almost zero transmission at 15 Hz, confirming the effectiveness of the EDM in regulating low-frequency Rayleigh waves at sub-wavelength scales (see Fig. 10(d)). With EDMs ($\eta_2, \eta_3 > 0$), Rayleigh waves can still propagate through at 6 Hz, but large loss factors significantly reduce transmission (see the left panels of Figs. 10(e-g)). Unlike a non-dissipative metasurface, which directly scatters off the incident Rayleigh wave at 15 Hz, the EDM interacts with the incident wave and dissipates the energy. This phenomenon is clearly observed in the middle panels of Fig. 10(g). However, higher damping results in less energy dissipation within the EDM and greater conversion of Rayleigh waves to bulk waves at 23 Hz, thereby increasing transmitted energy (see the right panels of Figs. 10(e-g)).

This FRF analysis aligns with the equivalent model predictions in Fig. 9, demonstrating

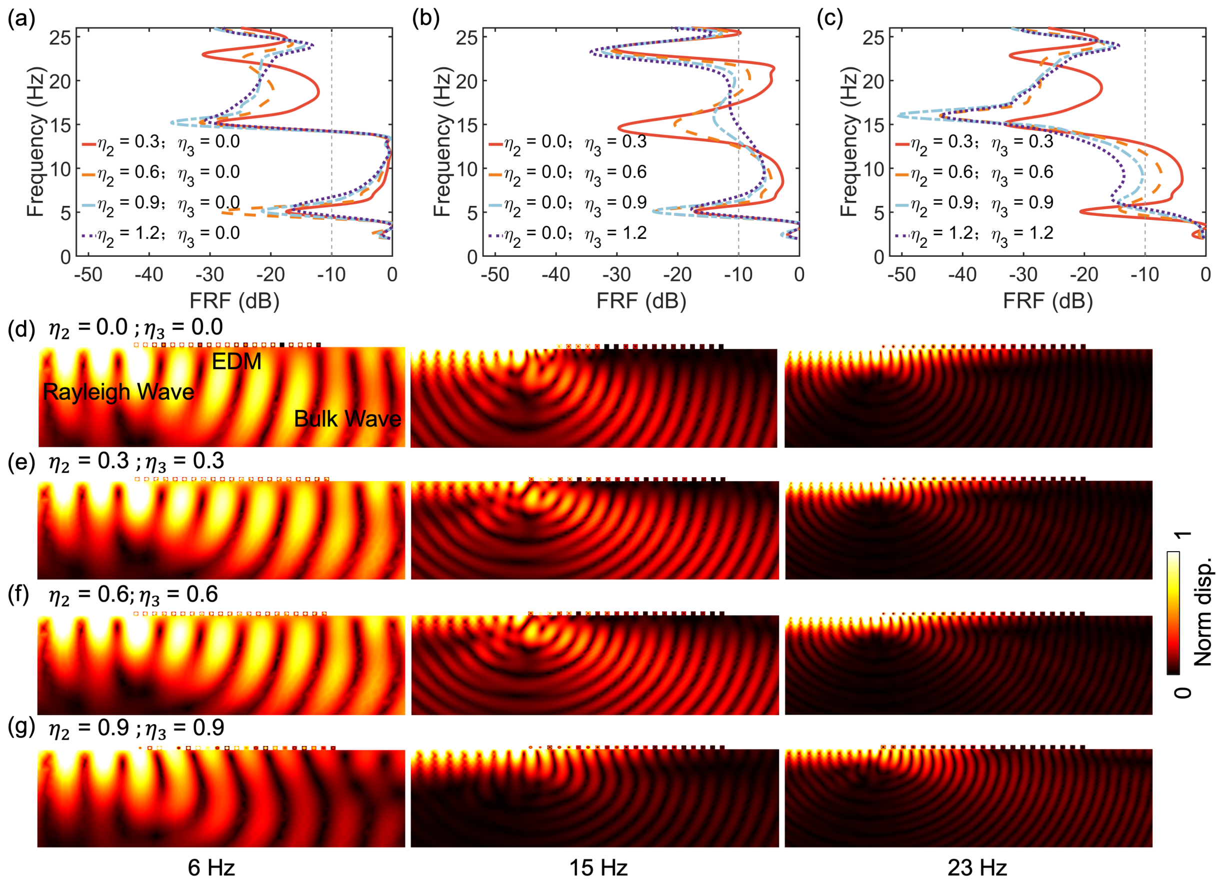

Figure 10: The EDM wave scattering field of the actual structure with three resonators cavity and the FRF under different loss factors: (a) $\eta_2 = 0.3, 0.6, 0.9, 1.2$; (b) $\eta_3 = 0.3, 0.6, 0.9, 1.2$; and (c) $\eta_2 = \eta_3 = 0.3, 0.6, 0.9, 1.2$. The wave scattering field of an incident Rayleigh wave at frequencies of 6 Hz, 15 Hz, and 23 Hz, with loss factors (d) $\eta_2 = \eta_3 = 0.0$, (e) $\eta_2 = \eta_3 = 0.3$, (f) $\eta_2 = \eta_3 = 0.6$, and (g) $\eta_2 = \eta_3 = 0.9$. The color scale indicates the elastic strain energy density level.

the EDM's effectiveness at sub-wavelength scales. These findings indicate that η_2 primarily affects the low-frequency stopband, while η_3 primarily affects the high-frequency stopband. Their combined effect achieves significant wave energy absorption and stopband formation over a broad frequency range, ensuring the broadband absorption required for low-frequency vibration isolation.

5. Rayleigh waves in media with spatially slow-varying EDMs and their applications

5.1. Rayleigh waves in spatially slow-varying EDMs

In previous sections, we developed a theoretical framework for describing Rayleigh waves by incorporating a uniform EDM composed of local resonators. However, a uniform arrangement often leads to significant wave reflection and bulk wave scattering, especially near the

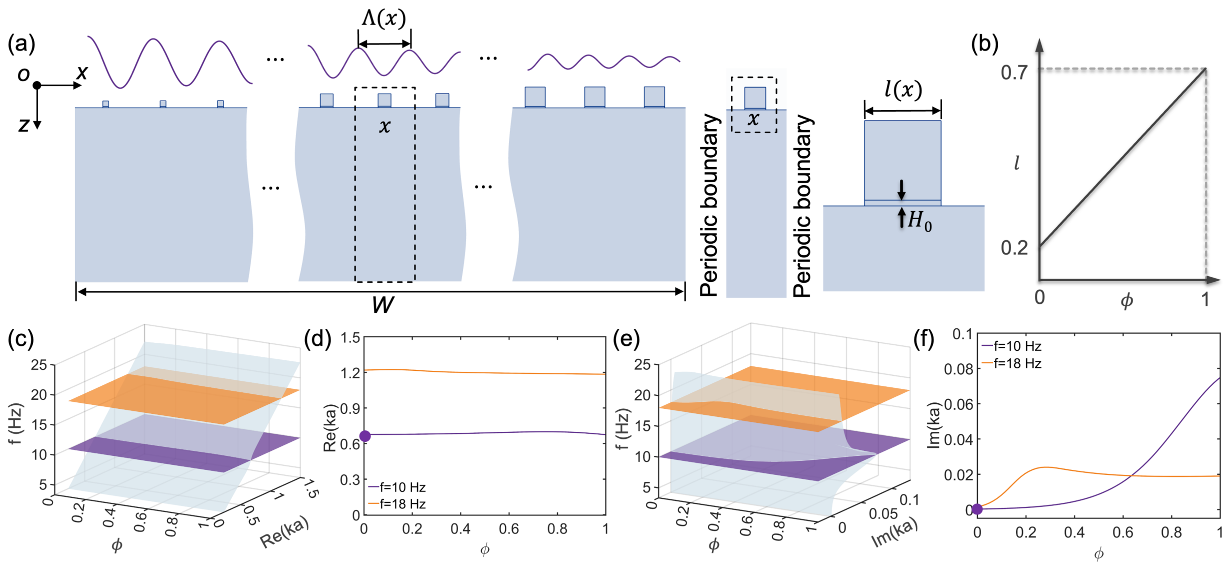

Figure 11: Principle of the adiabatic evolution of Rayleigh waves within a spatially slow-varying damping system. (a) Schematic diagram illustrating surface wave propagation in a spatially slow-varying EDM. (b) Variation of the side length of the resonator l as a function of the normalized spatial coordinate $\phi = x/W$. (c) The real part of the dispersion surface for Rayleigh waves overlaid with frequency planes corresponding to excitation frequencies of 10 Hz (purple) and 18 Hz (orange). (d) Curves representing the intersections of the frequency planes and the real part of the dispersion surface are depicted in (c). (e) The imaginary part of the dispersion surface for Rayleigh waves, with frequency planes at excitation frequencies of 10 Hz (purple) and 18 Hz (orange). (f) Curves showing the intersections of the frequency planes and the imaginary part of the dispersion surface described in (e).

resonant frequency. These reflected Rayleigh waves and scattered bulk waves may give rise to unexpected issues in engineering applications, such as in surface acoustic wave devices.

To address this issue, we propose a spatially slow-varying EDM that acts as a perfect absorber for broadband Rayleigh waves, functioning as a "rainbow surface absorber" (see Fig. 11(a)). Adiabatic conditions are essential in this design to ensure smooth wave propagation, minimizing reflections and scattering caused by abrupt variations in resonator properties. In this section, we first conduct a local unit cell analysis and explain its application for predicting wave propagation in the spatially slow-varying system [64, 63, 66, 73]. We then verify the wave behavior predicted from this analysis in both the frequency domain and time domain. Finally, we design a boundary absorber and a Rayleigh wave amplitude modulator based on these results. Here, single-resonant EDMs are used for verification, as shown in Fig. 1(a), but the paradigm is the same as that for multi-resonant EDMs.

In Fig. 11(a), we present a schematic diagram illustrating wave propagation in a spatially slow-varying EDM on a semi-infinite substrate. The EDM comprises 100 resonators to guarantee adiabatic conditions, which will be validated a posteriori. The side width of resonators increases from 0.2 m to 0.7 m as x varies from 0 to $W = 200$ a, as illustrated in Fig. 11(b). Under the adiabatic conditions, the Rayleigh wave propagates without scattering, as shown in Fig. 11(a). However, along the x axis, the wavelength $\Lambda = 2\pi/k$ is no longer a constant. The wavenumber $k(\phi)$ becomes a function that changes continuously from left to right, and $k(\phi)$ at normalized position $\phi = x/W$ can be determined by performing the local unit cell analysis.

For the local unit cell analysis, we first obtain the dispersion surface, a function of $k(f, \phi)$, of the Rayleigh wave by sweeping ϕ and f. The real and imaginary parts of this function are shown in Figs. 11(c) and 11(e), respectively. We then plot frequency planes at 10 Hz and 18 Hz (purple for 10 Hz and orange for 18 Hz). The intersection of these frequency planes and the dispersion surfaces provides the wavenumber function $k(\phi)$, as shown in Figs. 11(d) and 11(f). The real part of wavenumber $\mathrm{Re}(k(\phi))$ in Fig. 11(d) and the imaginary part of wavenumber $\mathrm{Im}(k(\phi))$ in Fig. 11(f) determine the local wavelength and decay factor at position x in Fig. 11(a). After obtaining the wavenumber function $k(\phi)$, the evolution of the Rayleigh wave can be predicted by the adiabatic theorem. If the initial eigenvalue, the wavenumber k of the Rayleigh wave, is excited with a frequency of 10 Hz (see the purple dot in Figs. 11(d) and 11(f) with $\phi = 0$), the Rayleigh wave will propagate from left to right without mode conversion. The local wavenumber and decay factor will follow the purple curves in Figs. 11(d) and 11(f).

5.2. Numerical verifications of Rayleigh waves in spatially slow-varying EDMs

Now we turn to the discussion of Rayleigh wave behavior in the frequency domain. The frequency domain response of the structure depicted in Fig. 11(a) at 10 Hz (top panel) and 18 Hz (bottom panel) is presented in Fig. 12(a). We observe that the Rayleigh wave decays along the x axis, with no observable bulk wave, reflected wave, or transmitted wave, thereby qualitatively verifying that the adiabatic condition is satisfied. The resulting Rayleigh wave will propagate undisturbed until being fully dissipated by EDMs.

To quantitatively analyze the evolution of the Rayleigh wave, the real part of displacement field w at $z = 3$ m is plotted in Figs. 12(b) and 12(d) for excitation frequencies of 10 Hz and 18 Hz, respectively. To extract the local wavenumber at various positions, we perform a wavelet transformation on the data presented in Figs. 12(b) and 12(d), which are displayed in Figs. 12(c) and 12(e). The wavenumber remains almost invariant along the x axis, with the normalized central wavenumber close to 0.7 at 10 Hz and 1.2 at 18 Hz, aligning well with the results in Fig. 11(d) from local unit cell analysis. To extract the decay factor $\mathrm{Im}(k)$ at different positions, we use the following

$$\mathrm{Im}(k(x)) = \frac{d}{dx} \ln\left(\frac{|w(x)|}{|w(0)|}\right), \tag{23}$$

where $|w(x)|$ is the magnitude of w displacement field at $z = 3$ m, $|w(0)|$ is the magnitude of w displacement at $z = 3$ m and $x = 0$ m, and the derivative is calculated by the finite difference method.

5.3. Applications of spatially slow-varying EDMs

The decay factors for the Rayleigh wave at excitation frequencies of 10 Hz and 18 Hz are shown in Fig. 12(f). At 10 Hz, the decay factor is small and increases slowly when

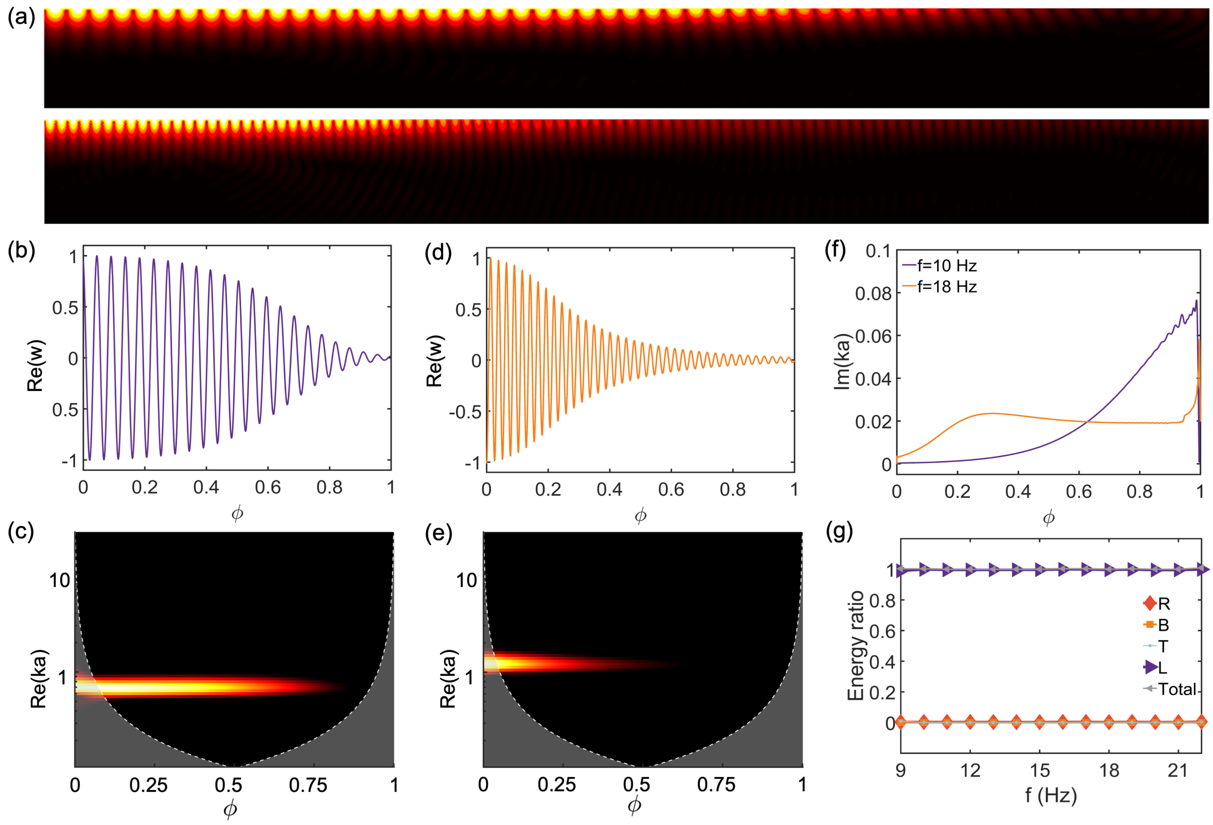

Figure 12: Verification of adiabatic evolution of Rayleigh waves in the frequency domain. (a) Frequency response of the Rayleigh wave under excitation from Eq. (18) at frequencies of 10 Hz (top panel) and 18 Hz (bottom panel). (b) The real part of vertical displacement distribution w along the cross-section at $z = -3$ m, shown in the top panel of (a). (c) Wavelet transforms of the data from (b). (d) The real part of vertical displacement distribution w along the cross-section at $z = -3$ m, depicted in the bottom panel of (a). (e) Wavelet transforms of the data from (d). (f) Local wavenumber function in relation to the normalized spatial coordinate ϕ. (g) Energy ratios of the reflected Rayleigh wave, transmitted Rayleigh wave, transferred bulk wave, energy dissipation within the EDM, and the total incident Rayleigh wave energy.

$\phi < 0.5$, but rises rapidly and becomes significant when $\phi > 0.5$. At 18 Hz, the decay factor increases to 0.2 after a short distance $\phi = 0.2$, and then remains constant, indicating exponential decay when $\phi > 0.2$. In addition, it can be observed that the decay factors in Fig. 12(f) agree well with those in Fig. 11(f), demonstrating that the decaying behavior of Rayleigh waves can be precisely predicted by a local unit analysis. It is important to note that the agreement between frequency response and unit cell analysis is valid only for systems that satisfy the adiabatic conditions. This coincidence verifies that the system satisfies the adiabatic conditions a posteriori. The resulting perfect energy dissipation proves its potential as a broadband Rayleigh wave absorber. As shown in Fig. 12(a), the Rayleigh wave is perfectly absorbed by the slowly varying EDM at both 10 Hz and 18 Hz. Finally, we perform an energy analysis of this system. The energy ratios for different waves at various frequencies are calculated as per the method in Section 2, shown in Fig. 12(g). From 9 Hz

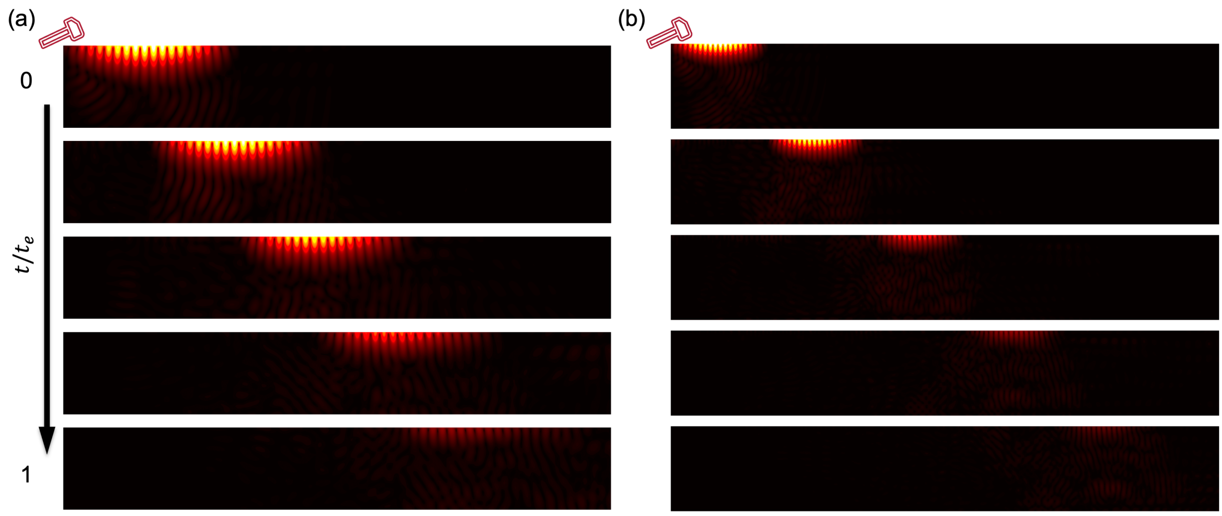

Figure 13: Verification of adiabatic evolution of Rayleigh waves in the time domain: (a) At 10 Hz. (b) At 18 Hz.

to 22 Hz, the energy ratio absorbed by resonators equals the incident energy ratio, while the energy ratios of other waves remain zero. Thus, this Rayleigh wave absorber operates perfectly over a broad frequency range.

Next, we turn to discussing the Rayleigh wave behavior in the time domain. For the excitation frequencies of 10 Hz and 18 Hz, the corresponding time evolution processes from initial time 0 to end time t_e are shown in Figs. 13(a) and 13(b), respectively. A Rayleigh wave in the time domain is excited by a distributed line displacement load at $x = 0$ with the profile

$$u = \left(re^{-kqz} + 2sqe^{-ksz}\right) g(t), \tag{24a}$$

$$w = q\left(re^{-kqz} - 2e^{-ksz}\right) g\left(t - \frac{1}{4f}\right), \tag{24b}$$

where $g(t)$ is a 10-cycles tone-burst signal defined as $g(t) = H\left(t - \frac{10}{f}\right)\left[1 - \cos\left(\frac{2\pi ft}{10}\right)\right]\sin(2\pi ft)$ with excitation frequency $f = 10$ Hz, and $H(t)$ is the Heaviside step function. In Fig. 13, we observe that the Rayleigh waves decay gradually without generating any reflected Rayleigh waves or scattered bulk waves at both frequencies. This verifies that our system can function as an effective Rayleigh wave absorber. Additionally, the wavelength of the Rayleigh wave remains nearly constant across different positions, consistent with the results shown in Figs. 11(c) and 11(e). The Rayleigh wave decays slowly at 10 Hz and rapidly at 18 Hz, but in both cases, it fully decays upon reaching the right boundary.

Based on the previous results of Rayleigh wave propagation in spatially slow-varying EDMs, we propose two applications. The first application is a boundary absorber designed for surface acoustic wave (SAW) devices. In traditional SAW devices, interdigital transducers generate and receive Rayleigh wave signals, but reflected Rayleigh waves from boundaries can adversely affect device performance. To mitigate these unwanted reflected waves, two

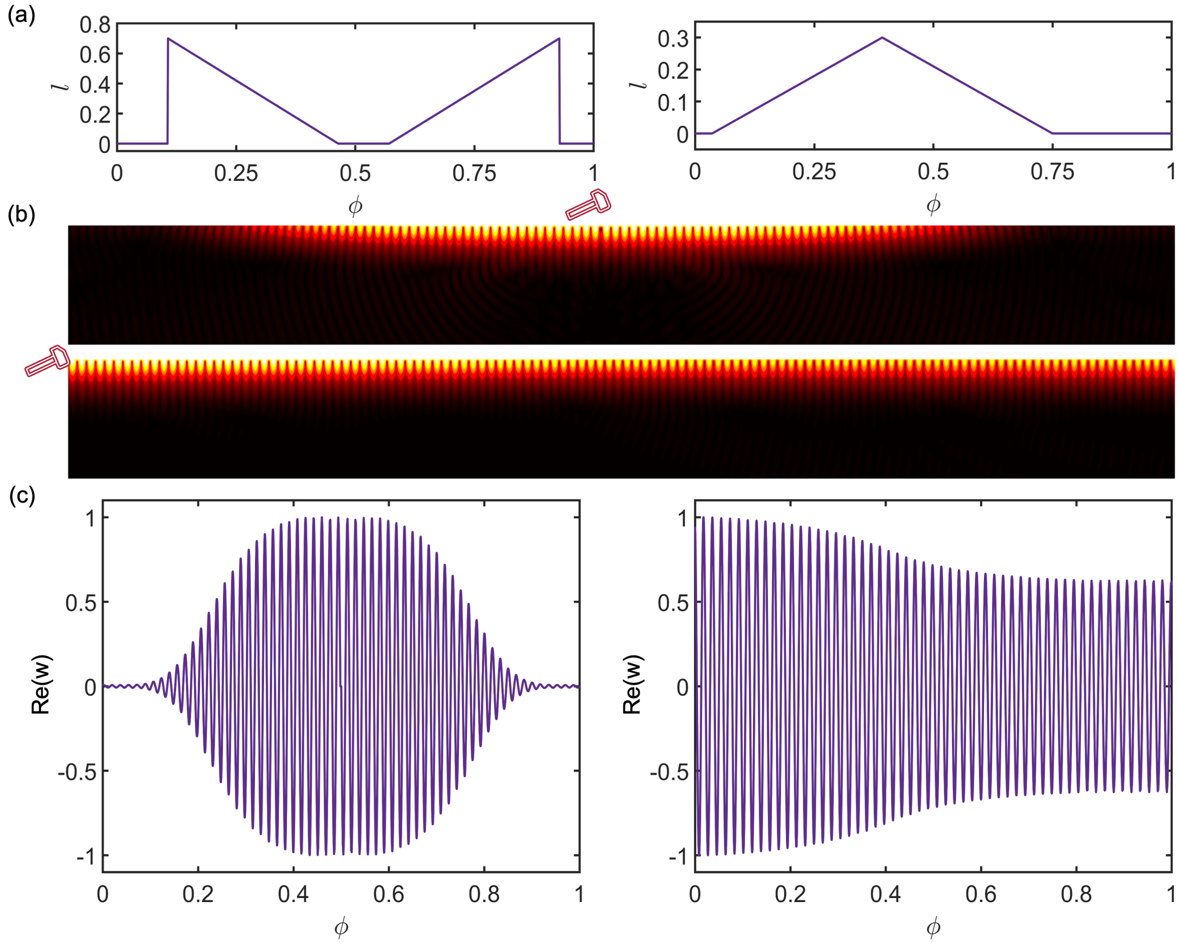

Figure 14: Application of spatially slow-varying EDMs as a perfect boundary absorber and a Rayleigh wave amplitude modulator. (a) Variation of the side length of the resonator l as a function of the normalized spatial coordinate ϕ for a boundary absorber (left) and an amplitude modulator (right). (b) Frequency response of the boundary absorber (top) and the amplitude modulator (bottom) under excitation described by Eq. (18) at a frequency of 10 Hz. (c) In the left (right) panel, the real part of vertical displacement distribution w, along the cross-section at $z = -3$ m of the boundary absorber (amplitude modulator), shown in the top (bottom) panel of (b).

space-varying EDMs, each consisting of 100 unit cells, are aligned in opposite directions. The function of side length l with respect to the normalized spatial coordinate ϕ for a boundary absorber is shown in the left panel of Fig. 14(a), where $l = 0$ means no resonators are attached. According to the previous results, the Rayleigh wave can be perfectly absorbed at the boundaries over a broad frequency range. To verify the results, we perform the FEM analysis in the frequency domain. A displacement load described in Eq. (24) is applied in the middle. For a 10 Hz excitation, the 2D frequency response is depicted in the top panel in Fig. 14(b), and the displacement field at $z = 3$ m is described in the left panel of Fig. 14(c). The results demonstrate that the Rayleigh wave is absorbed effectively at this frequency.

The second application is a Rayleigh wave amplitude modulator, which features a coneshaped EDM attached to the center of the substrate. The function of l with respect to ϕ for the Rayleigh wave amplitude modulator is shown in the right panel of Fig. 14(a). The same loading is applied on the left side of the substrate. For an excitation frequency of 10 Hz, the 2D frequency response is shown in the bottom panel of Fig. 14(b), and the displacement field at $z = 3$ m is illustrated in the right panel of Fig. 14(c). Here, the maximum side length l is set to a small value of 0.3, so the Rayleigh wave cannot be completely attenuated to zero but can be reduced to a finite value. By adjusting the maximum value of l, different output amplitudes of the Rayleigh wave can be achieved. Additionally, the introduction of active devices can enable time-dependent adjustments of stiffness, mass, and damping, allowing for real-time modulation of the Rayleigh wave.

6. Conclusion

In this study, we propose a novel EDM to effectively mitigate low-frequency broadband Rayleigh waves and their scattered components. Initially, we incorporate a single resonator array within the EDM to achieve Rayleigh wave mitigation over a narrow frequency range. However, the introduction of the EDM induced scattered waves and energy dissipation, prompting us to develop a comprehensive energy analysis framework to quantify the contributions of each wave component. This analysis provides critical insights for optimizing EDM design and improving wave control strategies.

To extend the applicability of EDMs, we integrate multiple resonators into the design, achieving subwavelength-scale broadband Rayleigh wave mitigation across low frequencies. The incorporation of spatially slow-varying EDMs further eliminates scattered waves, enabling perfect Rayleigh wave absorption over a broad frequency range. To address the absence of established theories for such systems, we develop a local unit cell analysis method grounded in the adiabatic theorem. This method facilitates precise predictions of wave behavior, unlocking innovative design opportunities such as perfect rainbow absorbers and Rayleigh wave modulators. ~~To address broader applications, we extend the design to incorporate multiple resonators, achieving subwavelength-scale, broadband, and low-frequency Rayleigh wave mitigation. Further, we introduce a spatially slow-varying EDM to eliminate scattered waves, enabling perfect Rayleigh wave absorption across a broad frequency range. Given the lack of established theories for wave behavior in such systems, we propose a local unit cell analysis method based on the adiabatic theorem, allowing precise predictions of wave evolution and facilitating innovative designs, such as perfect rainbow absorbers and Rayleigh wave modulators. These findings highlight the significant potential of EDMs in advancing wave control and vibration suppression for engineering applications.~~

Despite these advancements, challenges remain. For instance, achieving perfect rainbow absorption under adiabatic conditions often requires a large number of resonators, leading to material inefficiency. Although the adiabatic condition is not strictly necessary, alternative approaches such as the theory of shortcut to adiabaticity [73, 80] could mitigate these constraints. Furthermore, determining the minimal EDM length required for perfect absorption beyond adiabatic conditions poses an open question. For perfect absorption beyond the adiabatic conditions, an absorption inequality suggests that the EDM length must exceed a certain threshold determined by a length function related to the resonator parameters, based on the principles of causality and the Kramers-Kronig relationship [81, 82]. Absorption inequalities derived in acoustics and electrodynamics suggest a lower bound related to resonator parameters, but their adaptation to surface wave systems remains unexplored and warrants further study.

In conclusion, this study establishes a foundation for the practical application of EDMs in wave mitigation and provides a pathway for future research to refine these systems for enhanced efficiency and broader applicability.

CRediT authorship contribution statement

Siqi Wang: Writing – original draft, Writing – review & editing, Conceptualization, Methodology, Formal Analysis, Validation. **Zhigang Cao**: Writing – review & editing, Conceptualization, Validation, Supervision, Funding acquisition. **Qian Wu**: Writing – review & editing, Writing – original draft, Methodology, Conceptualization, Validation. **Jiaji Chen**: Writing – review & editing, Validation. **Yuanqiang Cai**: Writing – review & editing, Supervision, Funding acquisition. **Shaoyun Wang**: Writing – original draft, Writing – review & editing, Methodology, Formal Analysis, Software, Conceptualization, Validation. **Guoliang Huang**: Writing – review & editing, Writing – original draft, Conceptualization, Supervision.

Declaration of competing interest

The authors declare that there are no competing financial interests or personal relationships that could have influenced the work reported in this paper.

Data availability

No data was used for the research described in the article.

Acknowledgements

The work is supported by the National Natural Science Foundation of China (No. 51978611), the Science Fund for Distinguished Young Scholars of Zhejiang Province (No. LR21E080004), and the Center for Balance Architecture, Zhejiang University. The authors sincerely thank Dr. Yanzheng Wang for his valuable feedback and constructive suggestions, which greatly improved the quality of this paper.

Appendix A

The resultant of two polynomials $f(x) = a_n x^n + \cdots + a_0$, $g(x) = b_m x^m + \cdots + b_0$, $a_n \neq 0$, $b_n \neq 0$, $n > 0$, $m > 0$ equals to the determinant of their Sylvester matrix, namely

$$\mathrm{Res}(f, g) = \det[\mathrm{Syl}(f, g)],$$

where Sylvester matrix of two polynomials f, g is defined by

$$\mathrm{Syl}(f,g) = \begin{bmatrix} a_n & a_{n-1} & a_{n-2} & \cdots & 0 & 0 & 0 \\ 0 & a_n & a_{n-1} & \cdots & 0 & 0 & 0 \\ \vdots & \vdots & \vdots & \ddots & \vdots & \vdots & \vdots \\ 0 & 0 & 0 & \cdots & a_1 & a_0 & 0 \\ 0 & 0 & 0 & \cdots & a_2 & a_1 & a_0 \\ b_m & b_{m-1} & b_{m-2} & \cdots & 0 & 0 & 0 \\ 0 & b_m & b_{m-1} & \cdots & 0 & 0 & 0 \\ \vdots & \vdots & \vdots & \ddots & \vdots & \vdots & \vdots \\ 0 & 0 & 0 & \cdots & b_1 & b_0 & 0 \\ 0 & 0 & 0 & \cdots & b_2 & b_1 & b_0 \end{bmatrix},$$

where $a_n, \ldots, a_0$ are the coefficients of f and $b_m, \ldots, b_0$ are the coefficients of g.

The resultant can be used to solve polynomial equations. For equations

$$\begin{cases} 5x^2 - 6xy + 5y^2 - 16 = 0, \\ 2x^2 - (1 + y)x + y^2 - y - 4 = 0. \end{cases}$$

We define polynomials $f(x) = 5x^2 - 6xy + 5y^2 - 16$, $g(x) = 2x^2 - (1 + y)x + y^2 - y - 4$. Then we eliminate variable x, and we have

$$\mathrm{Res}(f,g) = \begin{vmatrix} 5 & -6y & 5y^2 - 16 & 0 \\ 0 & 5 & -6y & 5y^2 - 16 \\ 2 & -(1+y) & y^2 - y - 4 & 0 \\ 0 & 2 & -(1+y) & y^2 - y - 4 \end{vmatrix} = 32(y-2)(y-1)(y+1)^2.$$

The vanishment of resultant gives the solution $y = 2$, or $y = 1$, or $y = -1$.

When $y = 2$, the original equations are reduced as

$$\begin{cases} 5x^2 - 12x + 4 = 0, \\ 2x^2 - 3x - 2 = 0, \end{cases}$$

with the root of $x = 2$. Similarly, the root $x = -1$ for $y = 1$ whereas the root $x = 1$ for $y = -1$.

Appendix B: Second-Order Formulation of the System

The second-order governing equations for the longitudinal and transverse components of the system, as well as the surface dynamics, are presented here to describe the wave propagation behavior.

1. Longitudinal component ($\varphi(x,z)$)

The longitudinal wave component is governed by:

$$\frac{\partial^2 \varphi}{\partial z^2} - k(x)^2 \varphi + \frac{\omega^2}{c_L^2} \varphi = 0,$$

where $k(x)$ represents the local wavenumber and c_L is the longitudinal wave velocity.

2. Transverse Component ($\psi(x,z)$)

The transverse wave component satisfies:

$$\frac{\partial^2 \psi}{\partial z^2} - k(x)^2 \psi + \frac{\omega^2}{c_T^2} \psi = 0,$$

where c_T is the transverse wave velocity.

3. Surface Dynamics ($u_1(x)$)

The surface displacement dynamics, incorporating gradient mass and damping effects, is described by:

$$-m_{\text{eff}}(x)\omega^2 u_1(x) + ic_{\text{eff}}(x)\omega u_1(x) + k_1(x)\left(1 + i\delta_1\right)\left[u_1(x) - \frac{\partial \varphi(x,0)}{\partial z} - ik(x)\psi(x,0) - \psi_x^0(x,0)\right] = 0.$$

4. Boundary Conditions

At the surface $z = 0$, the longitudinal and transverse components are coupled through:

$$-\lambda k(x)^2 \varphi(x,0) + 2\mu i k(x) \frac{\partial \psi(x,0)}{\partial z} + (\lambda + 2\mu) \frac{\partial^2 \varphi(x,0)}{\partial z^2} = \frac{k_1(x)}{L}\left(u_1(x) - \frac{\partial \varphi(x,0)}{\partial z} - ik(x)\psi(x,0)\right),$$

$$\left(k(x)\psi(x,0)\right)_x + 2\frac{\partial^2 \varphi(x,0)}{\partial x \partial z} - k(x)^2 \varphi(x,0) + 2ik(x)\frac{\partial \varphi(x,0)}{\partial z} - \frac{\partial^2 \psi(x,0)}{\partial z^2} = 0.$$

These equations fully describe the second-order dynamics of the system.

Appendix C: Verification of the Adiabatic Condition for the Designed Metasurface with First-Order Formulation of the System

To analyze the mode coupling and verify whether the designed metasurface satisfies the adiabatic condition, the system is reformulated as a first order differential equation about space.

1. Longitudinal Component ($\varphi(x,z)$)

Introduce auxiliary variables for the longitudinal component:

$$\Phi_1 = \varphi, \quad \Phi_2 = \frac{\partial \varphi}{\partial z}.$$

The second-order equation becomes a set of first-order equations:

$$\frac{\partial \Phi_1}{\partial z} = \Phi_2, \quad \frac{\partial \Phi_2}{\partial z} = k(x)^2 \Phi_1 - \frac{\omega^2}{c_L^2}\Phi_1.$$

2. Transverse component ($\psi(x,z)$)

Similarly, for the transverse component:

$$\Psi_1 = \psi, \quad \Psi_2 = \frac{\partial \psi}{\partial z}.$$

The first-order formulation is:

$$\frac{\partial \Psi_1}{\partial z} = \Psi_2, \quad \frac{\partial \Psi_2}{\partial z} = k(x)^2 \Psi_1 - \frac{\omega^2}{c_T^2}\Psi_1.$$

3. Surface Dynamics ($u_1(x)$)

Introduce $U_2 = \frac{\partial u_1}{\partial x}$:

$$\frac{\partial u_1}{\partial x} = U_2.$$

The surface dynamics can then be expressed as:

$$\frac{\partial U_2}{\partial x} = \frac{1}{m_{\text{eff}}(x)}\left[-ic_{\text{eff}}(x)\omega u_1(x) - k_1(x)\left(1 + i\delta_1\right)\left(u_1(x) - \frac{\partial \varphi(x,0)}{\partial z} - ik(x)\psi(x,0)\right)\right].$$

4. Matrix Formulation

Combine all variables into a state vector:

$$\mathbf{X} = \begin{bmatrix} \Phi_1 \\ \Phi_2 \\ \Psi_1 \\ \Psi_2 \\ u_1 \\ U_2 \end{bmatrix},$$

then the governing equation for the wave propagation in the elastic half-space can be written as:

$$\frac{\partial \mathbf{X}}{\partial z} = \mathbf{A}(x)\mathbf{X},$$

where $\mathbf{A}(x)$ is the system matrix:

$$\mathbf{A}(x) = \begin{bmatrix} 0 & 1 & 0 & 0 & 0 & 0 \\ k(x)^2 - \frac{\omega^2}{c_L^2} & 0 & 0 & 0 & 0 & 0 \\ 0 & 0 & 0 & 1 & 0 & 0 \\ 0 & 0 & k(x)^2 - \frac{\omega^2}{c_T^2} & 0 & 0 & 0 \\ 0 & 0 & 0 & 0 & 0 & 1 \\ f_1(x) & f_2(x) & f_3(x) & f_4(x) & f_5(x) & f_6(x) \end{bmatrix},$$

where $f_1(x), f_2(x), \ldots, f_6(x)$ encode the coupling between surface, longitudinal, and transverse dynamics.Here, $k_x = \frac{\omega}{c_R}$ is the wavenumber of Rayleigh waves, and c_R is the Rayleigh wave velocity. To evaluate the mode coupling, we compute the spatial derivative of the system matrix $\frac{\partial \mathbf{A}}{\partial x}$ as follows:

$$\frac{\partial \mathbf{A}}{\partial x} = \lim_{\Delta x \to 0} \frac{\mathbf{A}(x + \Delta x) - \mathbf{A}(x)}{\Delta x}. \tag{25}$$

For numerical calculations, we use the finite difference approximation:

$$\frac{\partial \mathbf{A}}{\partial x} \approx \frac{\mathbf{A}(x + dx) - \mathbf{A}(x)}{dx}, \tag{26}$$

where dx is a small perturbation. The eigenvalues λ_i and eigenvectors v_i of the system matrix satisfy:

$$\mathbf{A}(x) v_i = \lambda_i v_i. \tag{27}$$

Using numerical methods, we extract the eigenvalues and eigenvectors to analyze the system behavior.

5. Adiabatic Condition

The adiabatic condition can now be analyzed based on the following criteria. The eigenvalue variation must satisfy:

$$\frac{\partial \lambda_i}{\partial x} \ll \lambda_i^2.$$

The mode coupling coefficient should satisfy:

$$\mathbf{C}_{ij} = \frac{\langle \mathbf{v}_i | \frac{\partial \mathbf{A}}{\partial x} | \mathbf{v}_j \rangle}{\lambda_i - \lambda_j}, \quad \text{with } |\mathbf{C}_{ij}| \ll 1.$$

These conditions ensure that the system remains adiabatic, with minimal scattering between modes. The computed mode coupling coefficients C_{ij} are visualized using a heatmap, as shown in Fig. 15. The calculation results confirm that this is an efficient adiabatic system with a heatmap of off-diagonal elements significantly smaller than 1. Rayleigh waves propagate smoothly without significant scattering or mode conversion, validating the effectiveness of metasurfaces as wideband Rayleigh wave absorbers.

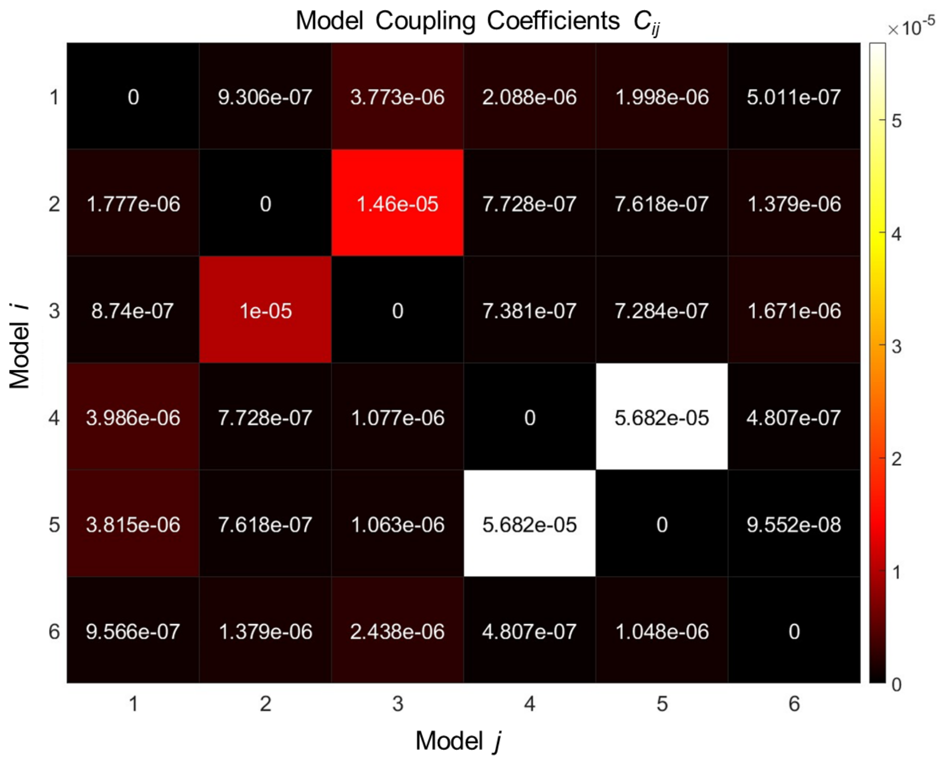

Figure 15: Mode coupling coefficients $|C_{ij}|$ visualized as a heatmap. A system satisfying the adiabatic condition should exhibit near-zero off-diagonal elements.

Appendix D: Energy Distribution Analysis with Normalized Incident Energy

Figure 16 presents the normalized energy distribution of different wave components, reflected Rayleigh wave (R), transferred bulk wave (B), transmitted Rayleigh wave (T), resonator absorption (L), and incident wave (I) at different frequencies f for a given loss factor η.

Consistent with the conclusions in Fig. 4, we observe that the energy conversion patterns of the Rayleigh waves remain similar after interaction with the metasurface structure. In the non-dissipative metasurface case (Fig. 16(a)), transmission energy significantly decreases within the bandgap frequency range, with most energy converting into bulk waves and reflections. This result is fully consistent with the bandgap dispersion analysis in Fig. 2(a), further demonstrating that the energy flux analysis effectively reveals wave transformation patterns and the energy distribution. As the loss factor increases (Figs. 16(b)-(c)), the absorption of the resonator becomes more pronounced, leading to enhanced energy dissipation and a redistribution of wave energy among different components. The comparison across different damping conditions highlights the transition of energy from transmitted waves to dissipation through the resonators. These results are consistent with the observations in Fig. 4, confirming that the metasurface effectively converts Rayleigh wave energy through reflection, bulk wave transformation, and resonator absorption.

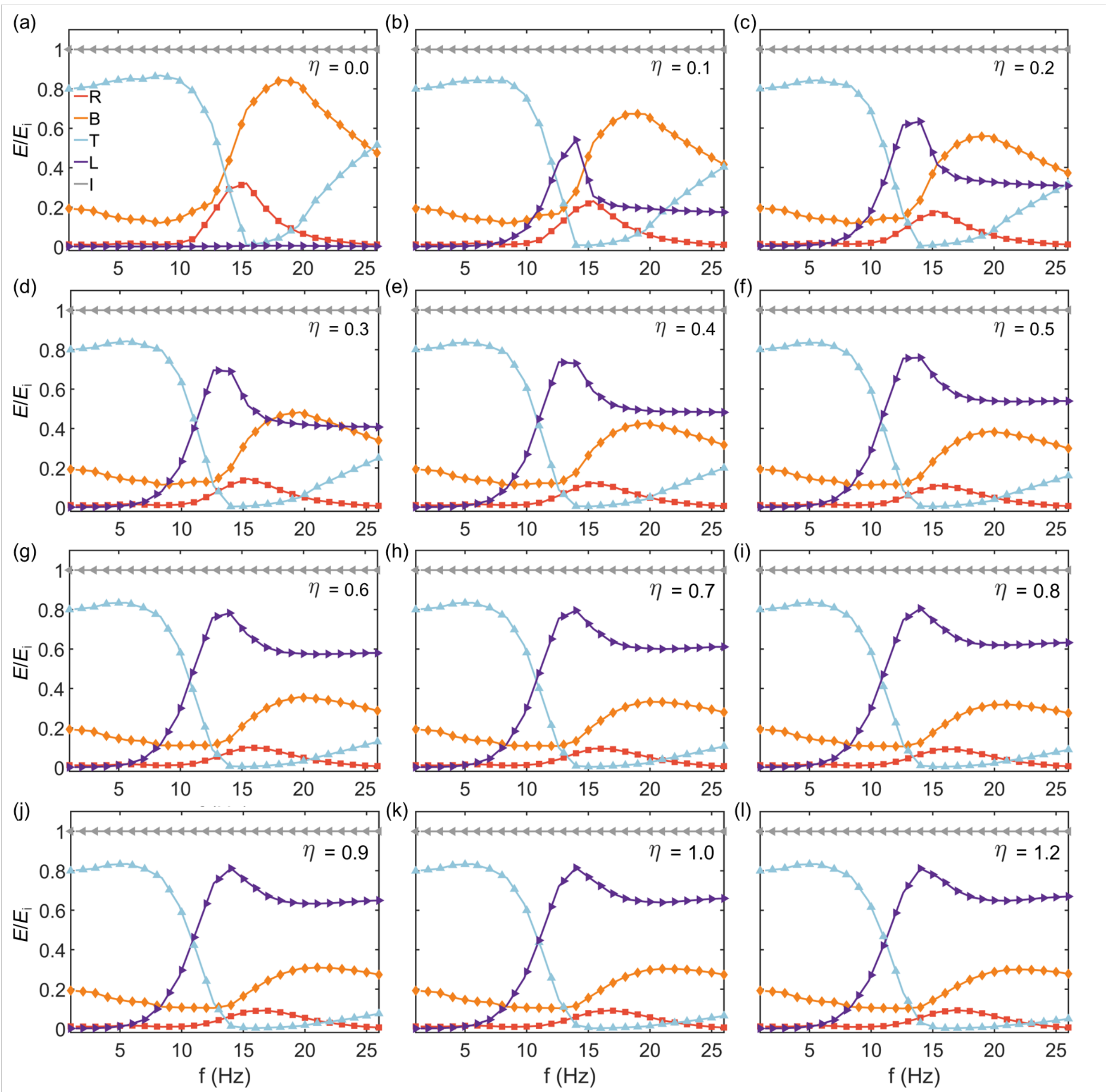

Figure 16: The energy (E) normalized by the incident energy is categorized as reflected Rayleigh wave (R), transferred bulk wave (B), transmitted Rayleigh wave (T), resonator absorption (L), and incident wave (I) with respect to different loss factors and different frequencies. S_1, S_2, S_3, and S_4 are the regions for calculating the energy of reflected Rayleigh wave, transmitted Rayleigh wave, bulk waves, and absorption by the EDM.

References

[1] Z. Liu, X. Zhang, Y. Mao, Y. Y. Zhu, Z. Yang, C. T. Chan, P. Sheng, Locally resonant sonic materials, science 289 (5485) (2000) 1734–1736.

[2] Q. Wu, X. Xu, H. Qian, S. Wang, R. Zhu, Z. Yan, H. Ma, Y. Chen, G. Huang, Active metamaterials for realizing odd mass density, Proceedings of the National Academy of Sciences 120 (21) (2023) e2209829120.

[3] M. I. Hussein, M. J. Leamy, M. Ruzzene, Dynamics of phononic materials and structures: Historical origins, recent progress, and future outlook, Applied Mechanics Reviews 66 (4) (2014) 040802.

[4] S. A. Cummer, J. Christensen, A. Alù, Controlling sound with acoustic metamaterials, Nature Reviews Materials 1 (3) (2016) 1–13.

[5] Y. F. Wang, Y. Z. Wang, B. Wu, W. Chen, Y.-S. Wang, Tunable and active phononic crystals and metamaterials, Applied Mechanics Reviews 72 (4) (2020) 040801.

[6] Y. Sun, Q. Han, T. Jiang, C. Li, Coupled bandgap properties and wave attenuation in the piezoelectric metamaterial beam on periodic elastic foundation, Applied Mathematical Modelling 125 (2024) 293–310.

[7] H. Huang, C. Sun, G. Huang, On the negative effective mass density in acoustic metamaterials, International Journal of Engineering Science 47 (4) (2009) 610–617.

[8] X. Zhou, X. Liu, G. Hu, Elastic metamaterials with local resonances: an overview, Theoretical and Applied Mechanics Letters 2 (4) (2012) 041001.

[9] S. H. Lee, O. B. Wright, Origin of negative density and modulus in acoustic metamaterials, Physical Review B 93 (2) (2016) 024302.

[10] R. Zhu, X. Liu, G. Hu, C. Sun, G. Huang, Negative refraction of elastic waves at the deep-subwavelength scale in a single-phase metamaterial, Nature communications 5 (1) (2014) 5510.

[11] A. Sukhovich, L. Jing, J. H. Page, Negative refraction and focusing of ultrasound in two-dimensional phononic crystals, Physical Review B—Condensed Matter and Materials Physics 77 (1) (2008) 014301.

[12] N. Contreras, X. Zhang, H. Hao, F. Hernández, Application of elastic metamaterials/meta-structures in civil engineering: A review, Composite Structures 327 (2024) 117663.

[13] G. W. Milton, M. Briane, J. R. Willis, On cloaking for elasticity and physical equations with a transformation invariant form, New journal of physics 8 (10) (2006) 248.

[14] H. Nassar, Y. Chen, G. Huang, Polar metamaterials: a new outlook on resonance for cloaking applications, Physical review letters 124 (8) (2020) 084301.

[15] M. Farhat, S. Guenneau, S. Enoch, Ultrabroadband elastic cloaking in thin plates, Physical review letters 103 (2) (2009) 024301.

[16] X. Zhang, Z. Liu, Superlenses to overcome the diffraction limit, Nature materials 7 (6) (2008) 435–441.

[17] X. Zhou, G. Hu, Superlensing effect of an anisotropic metamaterial slab with near-zero dynamic mass, Applied Physics Letters 98 (26) (2011).

[18] R. Zhu, X. Liu, G. Hu, C. Sun, G. Huang, A chiral elastic metamaterial beam for broadband vibration suppression, Journal of Sound and Vibration 333 (10) (2014) 2759–2773.

[19] Y. Xiao, J. Wen, D. Yu, X. Wen, Flexural wave propagation in beams with periodically attached vibration absorbers: Band-gap behavior and band formation mechanisms, Journal of Sound and Vibration 332 (4) (2013) 867–893.

[20] J. Lou, H. Fan, J. Yang, M. Xu, J. Du, Metamaterial design enabling simultaneous manipulation of rayleigh and love waves, Thin-Walled Structures 204 (2024) 112273.

[21] Y. Zeng, Y. Xu, H. Yang, M. Muzamil, R. Xu, K. Deng, P. Peng, Q. Du, A matryoshka-like seismic metamaterial with wide band-gap characteristics, International Journal of Solids and Structures 185 (2020) 334–341.

[22] A. Alzawi, M. H. El Naggar, Full scale experimental study on vibration scattering using open and in-filled (geofoam) wave barriers, Soil Dynamics and Earthquake Engineering 31 (3) (2011) 306–317.

[23] Z. Cao, Y. Cai, Isolation of train-induced ground-borne vibration by trenches on a poroelastic half-space, Journal of Engineering Mechanics 139 (5) (2013) 580–593.

[24] D. Ulgen, O. Toygar, Screening effectiveness of open and in-filled wave barriers: a full-scale experimental study, Construction and Building Materials 86 (2015) 12–20.
[25] X. Pu, Z. Shi, Broadband surface wave attenuation in periodic trench barriers, Journal of Sound and Vibration 468 (2020) 115130.
[26] D. Thompson, J. Jiang, M. Toward, M. Hussein, E. Ntotsios, A. Dijckmans, P. Coulier, G. Lombaert, G. Degrande, Reducing railway-induced ground-borne vibration by using open trenches and soft-filled barriers, Soil Dynamics and Earthquake Engineering 88 (2016) 45–59.
[27] D. J. Thompson, G. Kouroussis, E. Ntotsios, Modelling, simulation and evaluation of ground vibration caused by rail vehicles, Vehicle System Dynamics 57 (7) (2019) 936–983.
[28] Y. Xu, X. Pu, A. Palermo, A. Marzani, Y. Cai, Z. Cao, An analytical formulation to model geometric and resonant scattering of buried metabarriers for traffic-induced vibrations mitigation, International Journal of Solids and Structures 270 (2023) 112237.
[29] A. Palermo, S. Krödel, A. Marzani, C. Daraio, Engineered metabarrier as shield from seismic surface waves, Scientific reports 6 (1) (2016) 1–10.
[30] C. Lim, K. K. Żur, et al., Wide rayleigh waves bandgap engineered metabarriers for ground born vibration attenuation, Engineering Structures 246 (2021) 113019.
[31] Y.-Q. Cai, G.-Y. Ding, C.-J. Xu, Amplitude reduction of elastic waves by a row of piles in poroelastic soil, Computers and Geotechnics 36 (3) (2009) 463–473.
[32] G. M. Álamo, J. D. Bordón, J. J. Aznarez, G. Lombaert, The effectiveness of a pile barrier for vibration transmission in a soil stratum over a rigid bedrock, Computers and Geotechnics 110 (2019) 274–286.
[33] S. Brûlé, E. Javelaud, S. Enoch, S. Guenneau, Experiments on seismic metamaterials: molding surface waves, Physical review letters 112 (13) (2014) 133901.
[34] L. Meng, Z. Cheng, Z. Shi, Vibration mitigation in saturated soil by periodic pile barriers, Computers and Geotechnics 117 (2020) 103251.
[35] S. Wang, Z. Cao, Y. Xu, Z. Xiao, Z. Yuan, Y. Cai, C. Gou, Prediction and mitigation of train-induced vibrations of over-track buildings on a metro depot: Field measurement and numerical simulation, Journal of Vibration and Control 29 (23-24) (2023) 5413–5426.
[36] T. Sheng, G. B. Liu, X. C. Bian, W. X. Shi, Y. Chen, Development of a three-directional vibration isolator for buildings subject to metro-and earthquake-induced vibrations, Engineering Structures 252 (2022) 113576.
[37] D. Colquitt, A. Colombi, R. Craster, P. Roux, S. Guenneau, Seismic metasurfaces: Sub-wavelength resonators and rayleigh wave interaction, Journal of the Mechanics and Physics of Solids 99 (2017) 379–393.
[38] Y. Zeng, L. Cao, S. Wan, T. Guo, Y.-F. Wang, Q.-J. Du, B. Assouar, Y.-S. Wang, Seismic metamaterials: Generating low-frequency bandgaps induced by inertial amplification, International Journal of Mechanical Sciences 221 (2022) 107224.
[39] H. Zheng, L. Miao, P. Xiao, K. Lei, Q. Wang, Novel metamaterial foundation with multi low-frequency bandgaps for isolating earthquakes and train vibrations, in: Structures, Vol. 61, Elsevier, 2024, p. 106070.
[40] R. Cai, Y. Jin, B. Djafari-Rouhani, S. Zhou, P. Chen, T. Rabczuk, H. Zhu, X. Zhuang, Attenuation of rayleigh and pseudo surface waves in saturated soil by seismic metamaterials, Computers and Geotechnics 165 (2024) 105854.
[41] X. Pu, A. Palermo, A. Marzani, Lamb's problem for a half-space coupled to a generic distribution of oscillators at the surface, International Journal of Engineering Science 168 (2021) 103547.
[42] X. Pu, A. Palermo, Z. Cheng, Z. Shi, A. Marzani, Seismic metasurfaces on porous layered media: Surface resonators and fluid-solid interaction effects on the propagation of rayleigh waves, International Journal of Engineering Science 154 (2020) 103347.
[43] C. He, S. Zhou, X. Li, H. Di, X. Zhang, Forest trees as a natural metamaterial for surface wave attenuation in stratified soils, Construction and Building Materials 363 (2023) 129769.
[44] Z. Chen, G. Wang, C. Lim, Artificially engineered metaconcrete with wide bandgap for seismic surface wave manipulation, Engineering Structures 276 (2023) 115375.

[45] A. Ni, Z. Shi, Q. Meng, Broadband surface wave attenuation in porous soil by elastic metasurfaces, International Journal of Mechanical Sciences 264 (2024) 108838.

[46] K. Zhang, J. Yu, H. Liu, B. Ding, Z. Deng, Low-frequency and wide bandgap seismic metamaterials for rayleigh wave attenuation, Engineering Structures 296 (2023) 116948.

[47] Y. Xu, Z. Cao, K. Cui, Y. Cai, X. Pu, Tunable metasurfaces for seismic love wave manipulation: A theoretical study, International Journal of Mechanical Sciences 251 (2023) 108327.

[48] A. Palermo, B. Yousefzadeh, C. Daraio, A. Marzani, Rayleigh wave propagation in nonlinear metasurfaces, Journal of Sound and Vibration 520 (2022) 116599.

[49] J. Lou, X. Fang, H. Fan, J. Du, A nonlinear seismic metamaterial lying on layered soils, Engineering Structures 272 (2022) 115032.

[50] B. Zhao, H. R. Thomsen, X. Pu, S. Fang, Z. Lai, B. Van Damme, A. Bergamini, E. Chatzi, A. Colombi, A nonlinear damped metamaterial: Wideband attenuation with nonlinear bandgap and modal dissipation, Mechanical Systems and Signal Processing 208 (2024) 111079.

[51] X. Xu, M. V. Barnhart, X. Fang, J. Wen, Y. Chen, G. Huang, A nonlinear dissipative elastic metamaterial for broadband wave mitigation, International Journal of Mechanical Sciences 164 (2019) 105159.

[52] X. Fang, J. Lou, Y. M. Chen, J. Wang, M. Xu, K. C. Chuang, Broadband rayleigh wave attenuation utilizing an inertant seismic metamaterial, International Journal of Mechanical Sciences 247 (2023) 108182.

[53] T. Zhao, W. Tian, L. Cao, Y. Xu, Z. Yang, Broadband absorption and asymmetric reflection of flexural wave by deep-subwavelength lossy elastic metasurface, Mechanical Systems and Signal Processing 200 (2023) 110578.

[54] T. Zhao, Z. Yang, W. Tian, L. Cao, Y. Xu, Deep-subwavelength elastic metasurface with force-moment resonators for abnormally reflecting flexural waves, International Journal of Mechanical Sciences 221 (2022) 107193.

[55] G. Huang, C. Sun, Band gaps in a multiresonator acoustic metamaterial (2010).

[56] Y. Chen, M. V. Barnhart, J. Chen, G. Hu, C. Sun, G. Huang, Dissipative elastic metamaterials for broadband wave mitigation at subwavelength scale, Composite Structures 136 (2016) 358–371.

[57] M. V. Barnhart, X. Xu, Y. Chen, S. Zhang, J. Song, G. Huang, Experimental demonstration of a dissipative multi-resonator metamaterial for broadband elastic wave attenuation, Journal of Sound and Vibration 438 (2019) 1–12.

[58] X. Pu, A. Marzani, A. Palermo, A multiple scattering formulation for elastic wave propagation in space–time modulated metamaterials, Journal of Sound and Vibration 573 (2024) 118199.

[59] J. Santini, X. Pu, A. Palermo, F. Braghin, E. Riva, Controlling surface acoustic waves (saws) via temporally graded metasurfaces, Available at SSRN 4774810 (2024).

[60] A. Palermo, P. Celli, B. Yousefzadeh, C. Daraio, A. Marzani, Surface wave non-reciprocity via time-modulated metamaterials, Journal of the Mechanics and Physics of Solids 145 (2020) 104181.

[61] Q. Wu, H. Chen, H. Nassar, G. Huang, Non-reciprocal rayleigh wave propagation in space–time modulated surface, Journal of the Mechanics and Physics of Solids 146 (2021) 104196.

[62] Q. Wu, X. Zhang, P. Shivashankar, Y. Chen, G. Huang, Independent flexural wave frequency conversion by a linear active metalayer, Physical Review Letters 128 (24) (2022) 244301.

[63] E. Riva, M. I. Rosa, M. Ruzzene, Edge states and topological pumping in stiffness-modulated elastic plates, Physical Review B 101 (9) (2020) 094307.

[64] M. I. Rosa, R. K. Pal, J. R. Arruda, M. Ruzzene, Edge states and topological pumping in elastic lattices with periodically modulated coupling, arXiv preprint arXiv:1811.02637 (2018).

[65] H. Chen, H. Zhang, Q. Wu, Y. Huang, H. Nguyen, E. Prodan, X. Zhou, G. Huang, Creating synthetic spaces for higher-order topological sound transport, Nature communications 12 (1) (2021) 5028.

[66] S. Wang, Z. Hu, Q. Wu, H. Chen, E. Prodan, R. Zhu, G. Huang, Smart patterning for topological pumping of elastic surface waves, Science Advances 9 (30) (2023) eadh4310.

[67] Y. Shen, P. Jiang, F. Liu, Y. Xu, Z. Yang, Flexural edge waves and customizable local modes of circular plates with metasurface, Applied Mathematical Modelling 138 (2025) 115749.

[68] A. Vakulenko, S. Kiriushechkina, D. Smirnova, S. Guddala, F. Komissarenko, A. Alù, M. Allen, J. Allen,

A. B. Khanikaev, Adiabatic topological photonic interfaces, Nature Communications 14 (1) (2023) 4629.
[69] A. Colombi, V. Ageeva, R. J. Smith, A. Clare, R. Patel, M. Clark, D. Colquitt, P. Roux, S. Guenneau, R. V. Craster, Enhanced sensing and conversion of ultrasonic rayleigh waves by elastic metasurfaces, Scientific Reports 7 (1) (2017) 6750.
[70] X. Wu, Z. Wen, Y. Jin, T. Rabczuk, X. Zhuang, B. Djafari-Rouhani, Broadband rayleigh wave attenuation by gradient metamaterials, International Journal of Mechanical Sciences 205 (2021) 106592.
[71] Y. Xu, Y. Shen, F. Liu, L. Cao, Z. Yang, Modulated flexural edge waves in a plate with its free edge structured by an array of grooves, Journal of Sound and Vibration 536 (2022) 117173.
[72] J. Chen, Y. Chen, X. Xu, W. Zhou, G. Huang, A physics-guided machine learning for multifunctional wave control in active metabeams, Extreme Mechanics Letters 55 (2022) 101827.
[73] E. Riva, J. De Ponti, J. Marconi, F. Braghin, R. Ardito, A. Corigliano, Adiabatic limit for scattering-free waveguiding in space-graded arrays of micro-resonators, European Journal of Mechanics-A/Solids 104 (2024) 105162.
[74] Y. Xia, E. Riva, M. I. Rosa, G. Cazzulani, A. Erturk, F. Braghin, M. Ruzzene, Experimental observation of temporal pumping in electromechanical waveguides, Physical Review Letters 126 (9) (2021) 095501.
[75] S. J. Mitchell, A. Pandolfi, M. Ortiz, Metaconcrete: designed aggregates to enhance dynamic performance, Journal of the Mechanics and Physics of Solids 65 (2014) 69–81.
[76] R. Das, R. Kumar, S. L. Banerjee, P. P. Kundu, Engineered elastomeric bio-nanocomposites from linseed oil/organoclay tailored for vibration damping, RSC Advances 4 (103) (2014) 59265–59274.
[77] J. Rose, Ultrasonic Guided Waves in Solid Media, Cambridge University Press, 2014.
[78] Y. Long, J. Ren, H. Chen, Intrinsic spin of elastic waves, Proceedings of the National Academy of Sciences 115 (40) (2018) 9951–9955.
[79] A. Fishman, G. Elbaz, T. V. Varma, G. Shmuel, Third-order exceptional points and frozen modes in planar elastic laminates, Journal of the Mechanics and Physics of Solids 186 (2024) 105590.
[80] D. Guéry-Odelin, A. Ruschhaupt, A. Kiely, E. Torrontegui, S. Martínez-Garaot, J. G. Muga, Shortcuts to adiabaticity: Concepts, methods, and applications, Reviews of Modern Physics 91 (4) (2019) 045001.
[81] H. Y. Mak, X. Zhang, Z. Dong, S. Miura, T. Iwata, P. Sheng, Going beyond the causal limit in acoustic absorption, Physical Review Applied 16 (4) (2021) 044062.
[82] K. N. Rozanov, Ultimate thickness to bandwidth ratio of radar absorbers, IEEE Transactions on Antennas and Propagation 48 (8) (2000) 1230–1234.